

5. SITE 898¹

Shipboard Scientific Party²

HOLE 898A

Date occupied: 20 April 1993
Date departed: 24 April 1993
Time on hole: 3 days, 20 hr, 45 min
Position: 41°41.100'N, 12°7.380'W
Bottom felt (drill-pipe measurement at rig floor, m): 5290.3
Distance between rig floor and sea level (m): 11.32
Water depth (drill-pipe measurement from sea level, m): 5279.0
Total depth (from rig floor, m): 5631.80
Penetration (m): 341.50
Number of cores (including cores having no recovery): 36
Total length of cored section (m): 341.50
Total core recovered (m): 289.22
Core recovery (%): 84
Oldest sediment cored:
Depth (mbsf): 341.5
Nature: claystone
Age: late Oligocene
Measured velocity (km/s): 1.7

HOLE 898B

Date occupied: 24 April 1993
Date departed: 24 April 1993
Time on hole: 9 hr, 45 min
Position: 40°41.160'N, 12°7.380'W
Bottom felt (drill-pipe measurement at rig floor, m): 5289.1
Distance between rig floor and sea level (m): 11.42
Water depth (drill-pipe measurement from sea level, m): 5277.7
Total depth (from rig floor, m): 5294.50
Penetration (m): 5.40
Number of cores (including cores having no recovery): 1
Total length of cored section (m): 5.40
Total core recovered (m): 5.42
Core recovery (%): 100
Oldest sediment cored:
Depth (mbsf): 5.4
Nature: silt
Age: Pleistocene
Measured velocity (km/s): 1.5
Principal results: Site 898 is situated in the Iberia Abyssal Plain over an elliptical basement ridge within the ocean/continent transition (OCT) zone.

Geophysical modeling had predicted that the ridge lay within a part of the OCT, intermediate between thin oceanic crust to the west and thinned continental crust to the east, in which magnetic anomalies cannot be modeled by seafloor spreading. The site was one of a transect of sites across the OCT designed to study the petrological changes in the basement rocks within the OCT to identify the processes that accompanied continental breakup and the onset of steady-state seafloor spreading. APC and XCB cores were obtained from two holes that penetrated 342 m of Pleistocene to late Oligocene sediments. Coring and logging plans were terminated by the loss of about 3340 m of drill pipe. This meant that insufficient drill pipe remained on board the ship for us to core an adequate basement section at this site.

1. Unit I contains at least 260 turbidites that were deposited in the last 1.1 Ma; on average, one turbidite was deposited every 4000 yr.

2. A significant depositional hiatus starting in the middle Miocene, correlatable with a regional angular unconformity on seismic reflection profiles, may be related to a northwest-southeast compressional phase in the Betic Mountains of southern Spain and structural inversion in the Lusitanian Basin of Portugal.

Two lithologic units have been identified at Site 898.

1. Unit I (0-163.4 mbsf) is a Pleistocene to late Pliocene silty clay to clayey silt, silt, and fine sand with nannofossil clay. The unit mainly consists of terrigenous turbidites.

2. Subunit IIA (163.4-172.2 mbsf) is a middle Miocene silty clay to clayey silt with nannofossil clay and clay. The Subunit mainly consists of intensely bioturbated pelagic/hemipelagic sediments.

Subunit IIB (172.2-339.7 mbsf) is a middle Miocene to late Oligocene silty claystone to clayey siltstone and nannofossil claystone with claystone. The Subunit mainly consists of calcareous contourites and terrigenous turbidites.

The sedimentary section provides a discontinuous fossil record from the Pleistocene through the late Oligocene. Calcareous nannofossils are generally present. Planktonic and benthic foraminifers are abundant to common in the Pleistocene and late Pliocene deposits, but are less common below. An unconformity from middle Miocene to late Pliocene represents a 10-m.y. hiatus.

Acoustic formations 1A and 1B are widely recognized on multichannel seismic reflection profiles on the western Iberia margin and have been locally dated by previous drilling. At Site 898, acoustic formation boundary 1A/1B correlates with the middle Miocene to late Pliocene hiatus at 162 mbsf and with the top of Subunit IIA. Seismic profiles around the Leg 149 drill sites show a layer of westward/southwestward inclined reflectors within acoustic formation 1B. The shape and extent of this layer suggest that it is part of a contourite drift, the top of which may have been cored near the base of Hole 898A.

Many potential magnetic reversals were observed in the almost complete sequence of APC/XCB cores from 0 to 177 mbsf. At greater depths, the cores were too weakly magnetized. The Brunhes to Gauss sequence of chrons has been tentatively identified in the APC cores (0-133 mbsf). At the centimeter-scale, peaks in magnetic susceptibility values are associated with the terrigenous sandy layers in the turbidites of Unit I.

In-situ temperature measurements indicate that the vertical temperature gradient between the seafloor and 176 mbsf is about 41 °C/km and that the vertical conductive heat flow is about 61 mW/m². Physical property measurements on the sediments exhibit a small but steady increase in

¹Sawyer, D.S., Whitmarsh, R.B., Klaus, A., et al., 1994. *Proc. ODP, Init. Repts.*, 149: College Station, TX (Ocean Drilling Program).

²Shipboard Scientific Party is as given in list of participants preceding the contents.

density, seismic velocity, formation factor, and thermal conductivity, and a concomitant decrease in porosity, with depth.

Interstitial-water samples were obtained from Units I and II (3-336 mbsf). The pore-water chemistry (sulfate, alkalinity, ammonia, iron, manganese, calcium, magnesium, strontium, potassium, silica, chloride, and sodium) reflects the rapid deposition of the Pliocene-Pleistocene turbidites and the relatively slower deposition of the earlier sediments. The principal result is the surprisingly high sulfate concentration (up to 16 mM) in Subunit IIB. This has been attributed to a low sedimentation rate in the Miocene and Oligocene, low permeability, and the absence of reactive carbon. Concentrations of sulfate decrease rapidly from 3 to 71 mbsf as sulfate is consumed by reaction with organic carbon in Unit I.

Profiles of carbonate content vs. depth reflect a history of generally low biological productivity and deposition of hemipelagic sediment below the carbonate compensation depth (CCD), combined with delivery by turbidites of carbonate-rich material initially deposited above the CCD. Elevated organic carbon is found in Unit I (mean value 0.5%), whereas Unit II has much lower organic carbon. Relatively high concentrations of biogenic methane were encountered in headspace gas analyses of lithostratigraphic Unit I and Subunit IIA, but methane was essentially absent from all deeper sections.

BACKGROUND AND SCIENTIFIC OBJECTIVES

Site 898 (Fig. 1, "Site 897" chapter, "Background and Scientific Objectives" section, this volume) was one of a series of sites drilled during Leg 149 to elucidate the nature of the top of the crust (acoustic basement) within the ocean/continent transition (OCT) beneath the Iberia Abyssal Plain. The regional background to this and the other Leg 149 sites is presented elsewhere (see "Introduction" chapter, this volume; Whitmarsh, Miles, and Mauffret, 1990; Whitmarsh, 1993). Site 898 was chosen to sample a basement high located between the thin oceanic crust to the west and the weakly magnetized thinned continental crust to the east (see Fig. 4 in "Introduction" chapter, this volume). The site is located at the eastern edge of an intermediate zone of high magnetization and smooth acoustic basement (between the basement highs) that is located between the latter two crustal types. The basement high under the site is roughly elliptical in plan view with a steep northern slope, and its shape contrasts strongly with the linear north-south basement ridges and valleys at, and west of, Site 897 (Fig. 2, "Site 897" chapter, "Background and Scientific Objectives" section, this volume). On east-west seismic profiles, the basement high has an irregular, possibly fault-controlled, surface, whereas on a north-south profile, it has an almost flat, gently rounded surface. We expected this high to be a fault block consisting of thinned continental crust.

About 870 m of sediment overlies basement. By analogy with Site 398, 110 km east of Site 898, we expected to encounter ooze/chalk with turbidites over chalk, mudstone, and claystone (Sibuet, Ryan, et al., 1979). Before Leg 149, seismic reflection profiles traced back to Site 398 indicated that the basal sediments might be as old as early Late Cretaceous. A regional unconformity, which resulted from gentle folding that occurred during the Rif-Betic compressional phase in southern Spain and North Africa and which is clearly visible on seismic reflection profiles from the Iberia Abyssal Plain, was expected to occur at about 190 mbsf. In the vicinity of Site 898, the unconformity is marked by horizontal sedimentary reflectors that onlap low-angle, westward-dipping reflectors (Fig. 1). The sediments thicken to at least 1.7 s two-way traveltime (1.9 km) in the basin underlain by the smooth basement west of the site and to at least 1.8 s two-way traveltime (2.1 km) to the east. Although we anticipated that acoustic basement at Site 898 might contain continental rocks, the exact petrology of these rocks and the amount of any synrift igneous material was completely unknown.

OPERATIONS

After completing Site 897, we conducted a single-channel seismic reflection and magnetic survey of proposed Sites IAP-2 and IAP-3C to

confirm their locations (see "Site Geophysics" section, this chapter). We then sailed to Lisbon, Portugal, to change crews. Leg 149C began at 0700 hr, 19 April 1993, with the first line ashore (all times are given in Universal Time Coordinated [UTC]). We departed Lisbon at 1702 hr, 19 April, and sailed to Site 898. We deployed a Datasonics beacon at 40°40.934'N, 12°07.316'W. This location had been confirmed during the geophysical survey prior to the end of Leg 149B. After the ship was stabilized in dynamic positioning mode over the primary beacon, a second backup Datasonics beacon was deployed.

Hole 898A

An advanced hydraulic piston core (APC)/extended core barrel (XCB) bottom-hole assembly (BHA) was assembled and run to the seafloor. The precision depth recorder (PDR) indicated a water depth of 5294.4 m below the rig floor (mbrf). Core 149-898A-1H was taken with the bit at 5290.0 mbrf. Recovery was 9.25 m, and the liner had split. We continued coring despite the possibility of having missed the mud line. The water depth was taken to be 5290.3 mbrf. APC Cores 149-898A-1H to -14H were taken from 5290.3 to 5423.0 mbrf (0.0-132.7 mbsf), with 132.7 m cored and 133.38 m recovered (100.5% recovery; Table 1). Cores were oriented from Core 149-898A-4H on, using the Tensor orientation tool. The ADARA temperature shoe was run on Core 149-898A-12H. After Core 149-898A-14H, the core barrel became stuck, and we had to drill down around it; therefore, we switched to XCB coring.

XCB Cores 149-898A-15X to -36X were taken from 5423.0 to 5631.8 mbrf (132.7-341.5 mbsf), with 208.8 m cored and 155.38 m recovered (74.4% recovery). WSTP temperature measurements and water samples were taken at 5467.7 mbrf (177.4 mbsf) and 5515.9 mbrf (225.6 mbsf). XCB coring was terminated when the time per core had increased unduly and recovery had begun to decrease. At this site, we anticipated deploying a reentry cone, setting casing, and coring to basement. Hole 898A ended when the bit cleared the seafloor at 0845 hr on 24 April.

Hole 898B

The ship was offset 10 m to the north for a jet-in test and to obtain a mud-line core. However, the jet-in test had to be abandoned because of severe weather. We were experiencing a ship's heave of 14 ft (4.3 m) and large weight fluctuations on the drill string. Hole 898B was intended to obtain a complete mud-line core and only one additional APC core. Attempting the mud-line APC core was considered safe because the bit could stay above the seafloor. We positioned the bit at 5285.0 mbrf, and Hole 898B was spudded at 1201 hr, 24 April. We recovered 5.42 m of sediment in the core barrel. Therefore, the seafloor was taken to be at 5289.1 mbrf. Core 149-898B-1H was taken from 5289.1 to 5294.5 mbrf (0-5.4 mbsf).

Weather conditions deteriorated (Force 9 gale, 25-ft swells) as we began pulling out of the hole to begin reentry cone/casing operations. The APC/XCB BHA had been pulled to 3455 mbrf, when the drill string broke at the rig floor at 1730 hr on 24 April. We lost approximately 3.34 km of drill string. The two Datasonics beacons were recovered. We began inspecting all the joints in the recovered sections of the drill string, began assessing the total amount of usable drill pipe remaining aboard the ship, and waited for the weather to improve.

The site was abandoned when it became clear that insufficient usable drill pipe remained on board the ship to core an adequate basement section, which was the primary objective at this site.

SITE GEOPHYSICS

Geophysical Data near Site 898

Two time-migrated, multichannel seismic reflection profiles pass close to Site 898 (Fig. 2). They are the north-south Sonne Line 75-17 (Fig. 3) and the east-west Lusigal Line 12 (see Fig. 2, "Background

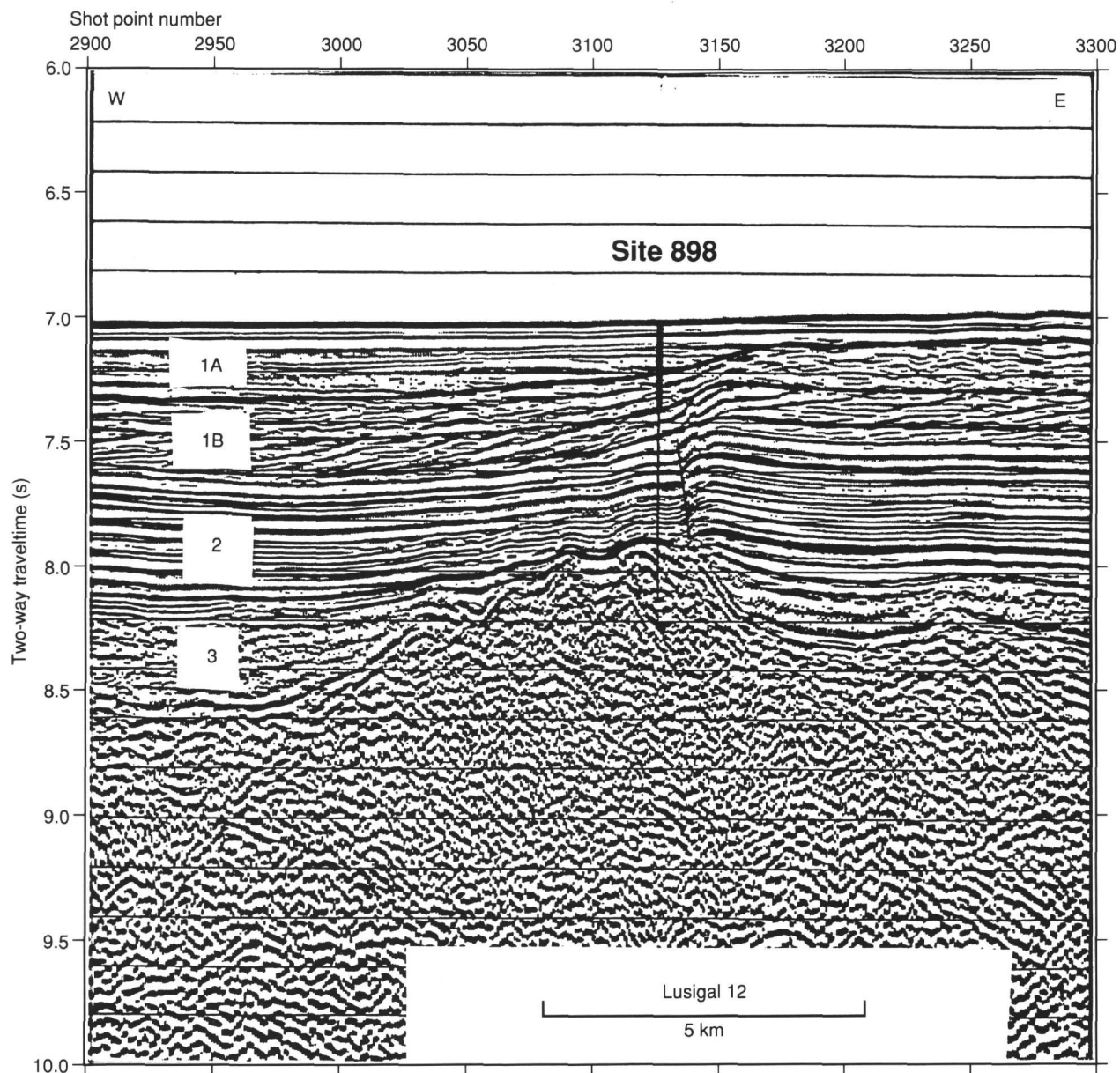


Figure 1. Migrated multichannel seismic reflection profile Lusigal 12 across Site 898 at SP 3126 (see Fig. 2 for location). Thin vertical line indicates the location and proposed penetration of the borehole; thick line indicates the penetration achieved. The enhanced lines on the section indicate boundaries between acoustic formations 1A, 1B, and 2, defined by Groupe Galice (1979) (see "Integration of Seismic Profiles with Observations from the Site" section, this chapter). The angular unconformity between acoustic formations 1A and 1B is described in the text. Vertical exaggeration is about 4:1.

and Scientific Objectives" section, this chapter) on which Site 898 is located. Site 898 is situated over a basement high that is 5 to 6 km wide in the east-west direction and 10 to 12 km wide in a north-south direction. The top of the high dips gently to the west and south and is about 900 ms two-way traveltime or 890 mbsf at its shallowest known point. The basement appears to be cut by three or four large normal faults that have a westerly component of dip; these are most clearly seen in Figure 1. Sediments fill the several small half-graben(?) basins, apparently formed by the faulting, on the high. Site 898 is located over the highest point of the basement. Sediments predicted to be Late Cretaceous in age cover the basement high, and older sediments onlap the high. The basin section to the west is thicker than that to the east. The sedimentary section at Site 898 consists of four main seismic units (Fig. 1). The topmost unit (0-210 ms two-way traveltime; Acoustic formation 1A of Groupe Galice, 1979) exhibits horizontal continuous parallel reflectors that we interpreted to be terrigenous turbidites. This

unit is substantially thicker to the west than to the east of the site. The second unit (210-360 ms two-way traveltime; top part of formation 1B of Groupe Galice, 1979) consists of discontinuous wavelike reflectors. The third unit (360-480 ms two-way traveltime; bottom part of formation 1B of Groupe Galice, 1979) consists of parallel inclined reflectors that dip to the west or southwest. The region in which these inclined reflectors are observed was mapped during Leg 149 (Fig. 4). The fourth unit (480-900 ms two-way traveltime; formation 2 of Groupe Galice, 1979) consists of parallel, continuous, high-amplitude reflectors. Formation 2 does not change thickness across the basement high. An apparently reverse fault, having an easterly component of dip, was observed in the sediment just to the east of Site 898. It extends from the east side of formation 2 (Fig. 1).

Magnetic data (Fig. 7, Site 897 chapter, "Site Geophysics" section, this volume; P.R. Miles, J. Verhoef, and R. MacNab, pers. comm., 1993) show that Site 898 is located on the southeastern side of a

Table 1. Coring summary for Site 898.

Core	Date (April 1993)	Time (UTC)	Depth (mbsf)	Length cored (m)	Length recovered (m)	Recovery (%)
149-898A-						
1H	21	0015	0.0-9.2	9.2	9.25	100.0
2H	21	0125	9.2-18.7	9.5	8.74	92.0
3H	21	0235	18.7-37.7	9.5	9.85	103.0
4H	21	0410	28.2-37.7	9.5	9.85	103.0
5H	21	0525	37.7-47.2	9.5	9.82	103.0
6H	21	0645	47.2-56.7	9.5	9.95	105.0
7H	21	0915	56.7-66.2	9.5	9.91	104.0
8H	21	1035	66.2-75.7	9.5	9.94	104.0
9H	21	1305	75.7-85.2	9.5	9.88	104.0
10H	21	1535	85.2-94.7	9.5	9.92	104.0
11H	21	1730	94.7-104.2	9.5	8.23	86.6
12H	21	2255	104.2-113.7	9.5	9.17	96.5
13H	22	0115	113.7-123.2	9.5	9.19	96.7
14H	22	0340	123.2-132.7	9.5	9.94	104.0
15X	22	0525	132.7-138.8	6.1	6.49	106.0
16X	22	0640	138.8-147.5	8.7	7.39	84.9
17X	22	0805	147.5-157.1	9.6	9.70	101.0
18X	22	0935	157.1-166.8	9.7	9.78	101.0
19X	22	1105	166.8-176.4	9.6	9.71	101.0
20X	22	1450	176.4-186.0	9.6	6.89	71.8
21X	22	1615	187.0-196.7	9.7	5.92	61.0
22X	22	1810	196.7-206.4	9.7	9.73	100.0
23X	22	2030	206.4-216.4	10.0	9.24	92.4
24X	22	2250	216.4-225.6	9.2	8.47	92.0
25X	23	0245	225.6-235.2	9.6	4.32	45.0
26X	23	0455	235.2-244.8	9.6	2.65	27.6
27X	23	0715	244.8-254.5	9.7	9.62	99.2
28X	23	0930	254.5-264.2	9.7	6.98	71.9
29X	23	1155	264.2-273.8	9.6	7.32	76.2
30X	23	1410	273.8-283.5	9.7	6.80	70.1
31X	23	1625	283.5-293.2	9.7	6.02	62.0
32X	23	1900	293.2-302.8	9.6	6.13	63.8
33X	23	2135	302.8-312.5	9.7	8.51	87.7
34X	23	2355	312.5-322.2	9.7	2.22	22.9
35X	24	0230	322.2-331.9	9.7	4.17	43.0
36X	24	0505	331.9-341.5	9.6	7.82	81.4
Coring totals				341.5	289.22	84.7
149-898B-						
1H	24	1035	0.0-5.4	5.4	5.42	100.0
Coring totals				5.4	5.42	100.0

magnetic anomaly high. The magnetic high is only slightly elongated in the north northwest-south southeast direction and is not parallel to the margin, as are most of the magnetic anomalies farther to the west. Beslier et al. (1993) and Whitmarsh, Miles, and Mauffret (1990) have interpreted seismic and magnetic profiles, respectively, to indicate that Site 898 is located over extended continental crust.

LITHOSTRATIGRAPHY

Introduction

The stratigraphic sequence recovered in Hole 898A consists of 340 m of Pleistocene to late Oligocene sediments and sedimentary rocks. Two lithostratigraphic units were recognized that were broadly similar to Units I and II at Site 897. The ages, averaged lithologic compositions, colors, facies and depositional environments, boundary depths, and cored intervals of Units I and II are summarized in Table 2 and Figure 5. Table 3 shows the colors associated with different lithologies.

Subsequent drilling at Site 900 suggested a regional stratigraphic correlation as shown in Figure 6. At Sites 897 through 900 the gross lithostratigraphy consists of a lower carbonate-rich contourite-turbidite-pelagite sequence and an upper turbidite-pelagite sequence. The two sequences contrast sharply in terms of evidence for reworking by contour currents (which is present only in the lower sequence) and in the abundance of siliceous allochems (which are virtually absent in the upper sequence).

Advanced hydraulic piston cores (APC) were taken down to Core 149-898A-14H (132.7 mbsf), and achieved very high recoveries (86%-104%). Subsequent drilling with an extended core barrel (XCB) obtained high recovery for the three cores that penetrated Unit I, but dropped in Unit II to about 70%, with a range from 27% to 101%. One

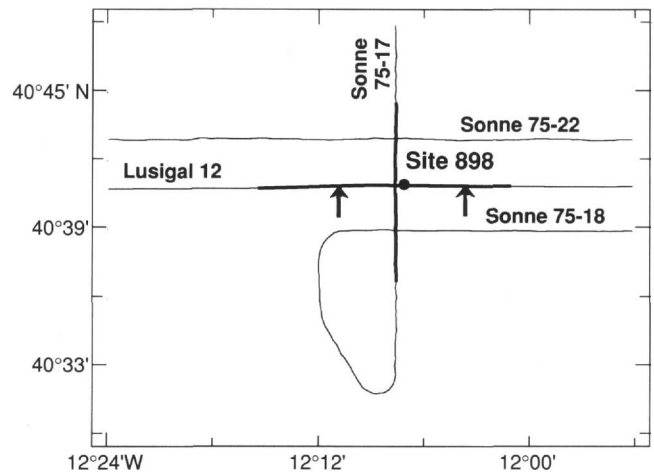


Figure 2. Multichannel seismic data and JOIDES Resolution Line 149-2 track chart in the vicinity of Site 898. Bold lines indicate the parts of Lusigal Line 12 and Sonne Line 75-17 shown in Figures 1 and 3, respectively. Line 149-2 replicated Lusigal Line 12 between the two arrows.

piston core was recovered in Hole 898B and contained sediments similar to Unit I, except for their brown color, which is presumed to reflect the presence of oxidized iron near the sediment/water interface (see "Inorganic Geochemistry" section, this chapter). Sediments from this core have been included in the description of Unit I at Hole 898 A.

Figure 7 shows that the proportion of sand and silt recovered is uniform at about 50% in the upper 12 cores. Below Core 149-898-12H, sand and silt content decrease to <10% at the Unit I/II boundary, from which point it remains relatively constant. Unit I contains greenish gray to greenish black siliciclastic turbidites, mostly capped by light gray nannofossil-rich hemipelagic/pelagic sediments. Subunit IIA consists of a thin (8.8 m) intensely bioturbated brown sequence of silty clay, nannofossil clay, and nannofossil ooze interpreted as pelagic and hemipelagic deposits. Subunit IIB contains light greenish-gray, fine-grained, carbonate-rich turbidites and contourites and darker, carbonate-poor, hemipelagic/pelagic deposits.

Figure 8 (see Table 4) is a plot of biostratigraphic age vs. depth for the sedimentary sequence penetrated at Site 898. Generalized sediment accumulation rates determined from Figure 8 vary from about 90 m/m.y. in Unit I to about 10 m/m.y. in Unit II.

Detrital grains observed in Units I and II at Site 898 are similar to those described for these units at Site 897. Two petrographically distinct clay-rich lithologies occur at this site. "Type 1" claystones and silty claystones contain carbonate in excess of a few percent and show no preferred orientation of the clay particles, which are very fine-grained. "Type 2" clay-rich lithologies contain virtually no carbonate; have coarse, yellow, birefringent clay crystals; and exhibit strong preferred clay orientation (for further description, see "Lithostratigraphy" section, "Site 897" chapter, this volume). A minor difference between Sites 897 and 898 is the occurrence of a few Type 2 claystones in Unit I at Site 898; clay-rich lithologies in Unit I at Site 897 consist entirely of Type 1 claystones.

Unit I

Cores 149-898A-1H through 149-898A-18X-4, 75 cm, and Core 149-898B-1H

Depth: Hole 898A, 0-163.35 mbsf; Hole 898B, 0-5.40 mbsf

Age: late Pleistocene to late Pliocene

General Description

Unit I extends from the seafloor to 163.35 mbsf (Fig. 5). Figure 9 shows that the core recovery for Unit I averages near 30% at Site 897,

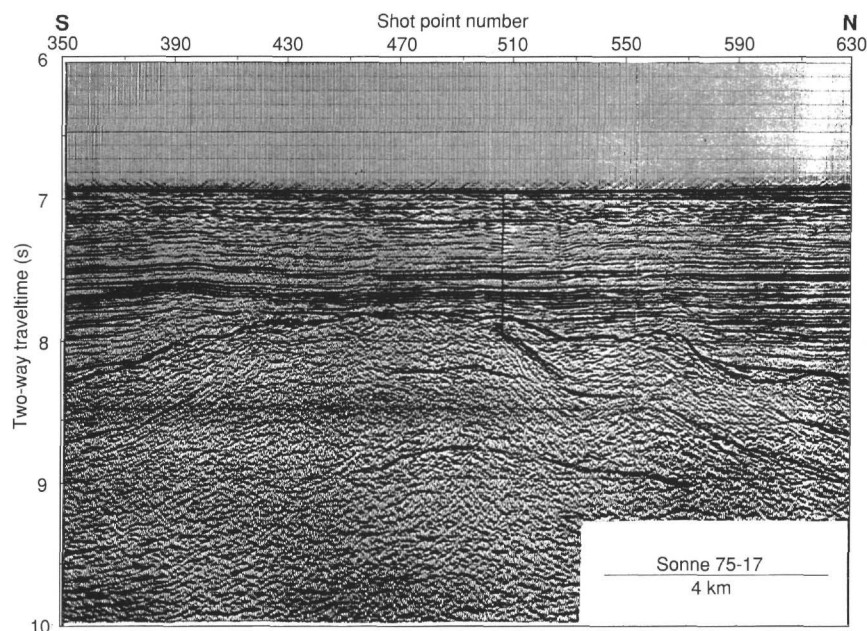


Figure 3. Migrated multichannel seismic profile Sonne Line 75-17 near Site 898. The location of this profile is shown in Figure 2. The projection of Site 898 is indicated by the vertical line. Vertical exaggeration is about 4:1.

while recovery at Site 898 approaches 100%. Corresponding to this increase in recovery, the observed percentage of sand in Unit I varies from about 11% at Site 897 to nearly 40% at Site 898. This difference in percentage of sand was interpreted as resulting from differences in coring methods that were employed at the two sites.

Core disturbance ranges from slight to very disturbed. Pronounced sediment flow occurs in most of the first 17 cores and decreases considerably in the remaining cores. Several layers of loosely consolidated sand and silt liquefied during drilling, destroying or disrupting sedimentary structures.

Silt to sand and silty clay to clayey silt dominate in Unit I; minor components include calcareous clay, clay, and nannofossil ooze (Table 2). Table 3 shows the ranges in colors for the different lithologies in Unit I. Much of the unit is greenish gray or dark greenish black. In contrast, light olive colors are common in the more calcareous and less terrigenous detritus-rich Unit II (Table 3).

Unit I consists of turbidites and associated pelagic/hemipelagic sediments. Individual turbidites range in thickness from about 5 cm to more than 1 m; as many as 40 were counted in one core (Core 149-898A-5H). These typically consist of a basal sand (less than 1 to greater than 150cm thick) that passes upward into silty clay, followed by nannofossil clay. Nannofossil ooze locally caps the sequence. The uppermost lithologies of the turbidites are typically bioturbated. Laminations and apparent cross-laminations occur in a few of the turbidite sands (Fig. 10).

Lithologies in the turbidites range from carbonate-poor (silty clays and clays) to carbonate-rich (nannofossil clay). Transitions between these lithologies occur over a span of a few meters and are manifested by color changes (shades of green in terrigenous lithologies and lighter grays in carbonate-rich sediments; Fig. 11).

Petrology

Applying the classification of Folk (1980), sands and silts of Unit I are subarkoses, arkoses, and lithic arkoses. Grain types in Unit I indicate derivation from a source area were mostly sedimentary, metamorphic, and, possibly, granitic rocks were exposed.

Most quartz grains are monocrystalline and some contain inclusions of rutile, tourmaline, and perhaps sillimanite. Polycrystalline quartz is a minor component, having equant subcrystals with mostly straight boundaries. The feldspar assemblage includes both twinned and untwinned plagioclase, and K-feldspar. Much of the plagioclase

is highly vacuolized, with minor sericite replacement. K-feldspar is principally microcline with very little alteration.

Carbonate rock fragments (CRFs) and metamorphic rock fragments (MRFs) are the main lithic components. CRFs are mostly micritic, but a substantial portion of sparry monocrystals also were observed. A minor component of distinctly rhombic particles, mostly in the silt fraction, is probably dolomite. Other sedimentary rock fragments include minor clay fragments and very rare pieces of chert. MRFs are quartz-mica aggregates derived from low-rank phyllites and schists.

Minor detrital components include abundant micas (muscovite, biotite, and possibly chlorite) that make up to 1% to 2% of the sand-silt fraction. Dense minerals present are mostly ultrastable species, such as zircon and yellow-brown to green tourmaline, with minor epidote, sphene (titanite), apatite, garnet, and green hornblende. Opaque detrital grains include black (magnetite and related minerals) and white (leucoxene) varieties.

Penecontemporaneous calcareous and siliceous marine skeletal debris (generally less than 10%) occurs in the sand/silt fraction, including foraminifers, sponge spicules, diatoms, radiolarians, dinoflagellates, and various nannofossils, including coccoliths and discoasters. In general, a negative correlation exists between the abundance of siliceous allochems and the carbonate content. Sand-sized and coarse silt-sized glauconite is a minor and ubiquitous component. Red brown organic detritus is occasionally noted in the coarse-silt fraction. All the terrigenous clastic material of Unit I is unconsolidated and contains no

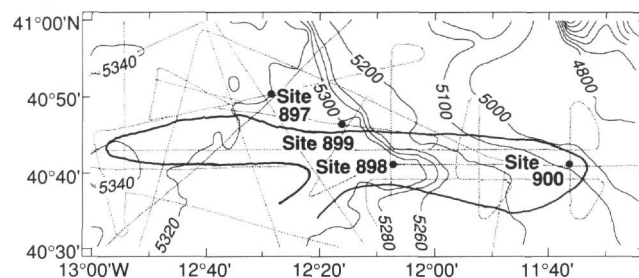


Figure 4. The distribution of the inclined reflector sequence in the vicinity of Leg 149 sites. Light lines are the seismic coverage on which the map is based. Fine dark lines are bathymetric contours. Bold line outlines the area in which the inclined reflector sequence was observed.

Table 2. Summary of ages, characteristics, facies, and depositional environments and occurrences of lithostratigraphic units and subunits at Site 898.

Unit	Age	Thickness (m)	Lithology	Percentage	Color	Facies and environment (total meters described)	Intervals Hole 898A ^a (mbsf)	Occurrence Hole 898A ^b
I	Pleistocene to late Pliocene	163.4	Clay	5	Gray/green	Terrigenous turbidites <i>Abyssal plain</i> [162.21]	Top = 0.0 Base = 163.35	1H-1 at 0 cm 18X-4 at 75 cm
			Nannofossil ooze	2				
			Nannofossil clay	15				
			Silty clay to clayey silt Silt and fine sand	39 39				
IIA	middle Miocene	8.8	Clay	15	Brown/pale orange	Intensely bioturbated Pelagic/hemipelagic sediments <i>Abyssal plain</i> [8.8]	Top = 163.35 Base = 172.17	18X-4 at 75 cm 19X-3 at 137 cm
			Nannofossil ooze	5				
			Nannofossil clay	20				
			Sily clay to clayey silt	50				
IIB	middle Miocene to late Oligocene	167.6	Claystone	15	Gray/green	Calcareous contourites/ Terrigenous turbidites <i>Abyssal plain</i> [117.65]	Top = 172.17 Deepest = 339.72 Base not observed	19X-3 at 137 cm 36X-CC at 32 cm
			Nannofossil chalk	<1				
			Nannofossil claystone	36				
			Silty clayst. to clayey siltst.	42 7				
			Siltstones and sandstone					

^aAlso Hole 899B; Top = 0.0; Deepest = 5.4.
^bAlso Hole 899B; -1H-1 at 0 cm to -1H-CC.

Table 3. Color variation of lithologies at Site 898.

Color	Munsell code	Sand	Sandy silt	Clayey silt/silty clay	Clay	Calc. clay/calc. silty clay	Nannofossil clay	Nannofossil ooze	Foraminifer sand	Silty diatom radiol. ooze
Dark gray	N4			o					*	
Medium gray	N5					o				
Medium light gray	N6							o *		*
Light gray	N7							o *		
Very light gray	N8						*	o *		
White	N9							* *		
Dark yellowish brown	10YR 4/2			■	■		■			
Very pale orange	10YR 8/2			■	■		■			
Brownish gray	5 YR 4/1				o					
Olive gray	5Y 4/1	o		o	o	o	o *	o		
Light olive gray	5Y 6/1	*		*	■		o			
Yellowish gray	5Y 8/1									
Grayish green	10GY 5/2		*	*						
Greenish black	5GY 2/1	o								
Dark greenish gray	5GY 4/1	o				o	o *			
Greenish gray	5GY 6/1		*	*	■		o *		*	
Light greenish gray	5GY 8/1			*			*	o	*	
Greenish black	5G 2/1	o	o							
Dark greenish gray	5G 4/1	*		o		o	o *			
Greenish gray	5G 6/1	*			o *	*				

Note: Unit I = o, Subunit IIA = ■, Subunit IIB = *

obvious post-depositional authigenic phases, except for generally minor framboidal pyrite.

Most of the clay-rich lithologies in Unit I contain a significant proportion of clay-sized (<4 μm) carbonate that consists largely of nannofossil debris. Clay minerals examined in smear slides are mostly <1 μm in diameter and show no evidence of crystal elongation or preferred orientation in undisaggregated pieces. Birefringence of small carbonate particles is low, and clay minerals in these rocks cannot be readily distinguished from clay-sized carbonate, except on the basis of color imparted, presumably, from trace amounts of iron oxides and organic matter. Carbonate-bearing clays with very fine clay particles and no evidence of preferred orientation in smear slides

have been designated Type 1. Carbonate contents in some Type 1 clay are low (<10%), but at least a small percentage of nannofossil debris is present.

A few clay-rich rocks in Unit I contain little carbonate and manifest pronounced orientation of the clay minerals within undisaggregated pieces observed in smear slides. These are Type 2 clay-rich lithologies and also larger (up to fine silt-sized) and more highly birefringent (up to first-order yellow) clay crystals.

On the basis of the petrographic similarities with lithologies at Site 897 and the close geographic proximity of the sites, the dominant clay minerals in Unit I are probably illite and kaolinite, with a lesser proportion of smectite (100% expandable).

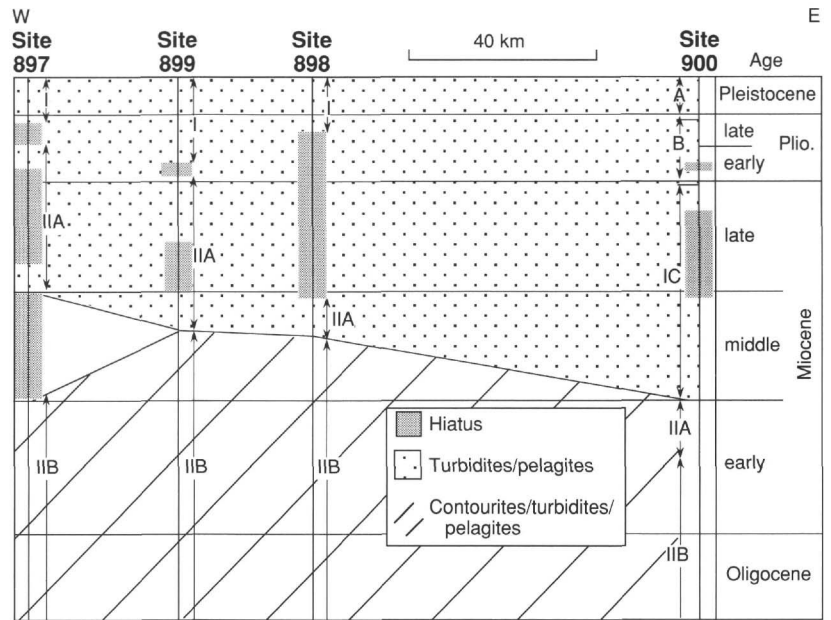


Figure 6. Regional stratigraphic correlation chart for Sites 897 to 900. The lower contourite-turbidite-pelagic sequence contains abundant siliceous allochems and reworked carbonate grains. The upper turbidite-pelagic sequence shows no evidence of reworking by contour currents.

Depositional Processes

The setting and processes, which we interpreted to be the deposition of Unit I, are similar to those described in more detail for Unit I, Site 897. The sediments are the product of turbidity current deposition on an abyssal plain. Pelagic sediments accumulated during periods of nonturbidity current deposition.

Compositional changes in both the pelagic and fine-grained terrigenous sediments of Unit I may record fundamental changes in oceanographic/climatic conditions. Increased carbonate content in turbidite lithologies may reflect periods of increased productivity in the water column, reduction in the flux of terrigenous material, or decreased carbonate dissolution. Alternatively, changes in the carbonate content of the turbidites may relate to changes in the location of the sediment source, with carbonate-rich turbidites derived from local submarine highs and more terrigenous turbidites from the continental margin, as suggested by Rothwell et al. (1992) for the Madeira Abyssal Plain.

Unit II

Section 149-898A-18X-4 at 74 cm to the base of Core 149-898A-36X
 Depth: 163.35-339.72 mbsf
 Age: middle Miocene to late Oligocene

General Description

The major lithologies in Unit II are silty clay/claystone to clay/claystone and nannofossil to calcareous clay/claystone. Minor lithologies are clay/claystone, nannofossil ooze/chalk, and calcareous or foraminifer-rich very fine sandstone to siltstone.

The top of Unit II is defined by a change in facies from the siliciclastic turbidite sequences of Unit I to uniform and/or mottled lithologies lacking significant sand or silt interbeds. The boundary between the units has been placed at the base of the last turbidite sand (at 74 cm in Section 149-898A-18X-4). A gradual change in color from gray to brown takes place across this boundary. The total thickness and age range of Unit II are not known because drilling ceased before reaching the lower boundary. Total recovery of Unit II was 127 m (about 71%).

Two Subunits were recognized in Unit II. Near the boundary between Units I and II, a gradational change occurs from poorly consoli-

dated to more lithified sediments. Beginning with Core 149-898A-18X, cores were split with a saw. Thus, lithologies in Subunit IIB have been described as "stones." The transition between Subunits IIA and IIB is marked also by a distinct increase in the number of thin beds (2-5 cm) of fine sand or silt and carbonate content. In addition, a significant amount (5%-15%) of siliceous microfossils appears for the first time (Fig. 12). The boundary between Subunits IIA and IIB has been placed at the top of this transitional interval, at the uppermost occurrence of laminated silt/sand beds (in Section 149-898A-19X-3 at 137 cm). The transition between Subunits IIA and IIB is characterized also by a gradual color change from brown to gray/green that occurs at the top of Subunit IIB across Intervals 149-898A-19X-3, 137 cm, through -19X-6, 95 cm.

Table 4. Biostratigraphic data used to constrain sediment accumulation rates for Site 898.

Code	Datum ^a	Age and range (Ma)	Depth range (mbsf)
1	<i>B. Emiliana huxleyi</i>	0.26	0.07-0.80
2	<i>T. Pseudoemilinia lacunosa</i>	0.46	14.76-17.94
3	<i>T. Reticulofenestra</i> sp.A (> 6.5 µm)	0.81	31.32-37.70
4	<i>B. Gephyrocapsa omega</i>	0.87	52.48-56.70
5	<i>B. Reticulofenestra</i> sp.A (> 6.5 µm)	0.98	66.98-75.70
6	<i>B. Gephyrocapsa</i> spp. (> 5.5 µm)	1.10	85.2-94.70
7	T. common <i>Helicosphaera sellii</i>	1.19	102.93-108.25
8	<i>B. Gephyrocapsa</i> spp. (> 5.5 µm)	1.37	119.54-122.89
9	<i>T. Calcidiscus macintyreii</i> (> 10 µm)	1.47	123.60-127.08
10	<i>T. Calcidiscus tropicus</i> (cir., ≥11.5 µm)	1.54	137.32-139.19
11	<i>B. Gephyrocapsa oceanica</i> (≥ 4.0 µm)	1.58	139.39-140.09
12	<i>B. Gephyrocapsa caribbeanica</i> (≥ 4.0 µm)	1.64	146.19-153.08
13	<i>T. Discoaster brouweri</i>	1.88	160.66-162.18
14	<i>B. Discoaster kugleri</i>	12.20	163.15-163.64
15	<i>T. Sphenolithus heteromorphus</i>	13.37	166.80-171.22
16	<i>T. Helicosphaera ampliapertura</i>	16.00	206.68-211.97
17	<i>T. Triquetrorhabdulus carinatus</i>	20.00	229.92-238.83
18	T. common <i>Cyclicargolithus abisectus</i>	24.70	261.48-264.65
19	<i>B. Sphenolithus ciperoensis</i>	29.40	326.37-337.30
20	Co-occurrence of <i>Sphaeroidinellopsis paenedehiscens</i> and <i>Globorotalia tosaensis</i>	3.00-3.1	153.08-157.10
21	<i>B. Globigerina nepenthes</i> and <i>Sphaeroidinellopsis disjuncta</i>	11.3-15.2	187.0-206.40
22	<i>T. Catapsydrax dissimilis</i>	17.6	216.4-224.87

^aT = top; B = bottom.

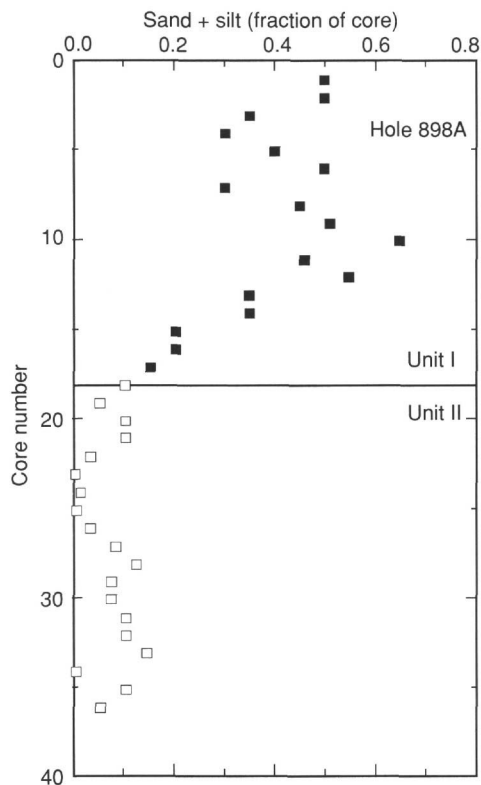


Figure 7. Sand and silt content in cores from Hole 898A. The proportion of sand and silt declines significantly through the lower one-third of Unit I.

Subunit IIA

Subunit IIA consists of a mottled and variegated monotonous sequence of dark yellowish brown to very pale orange nannofossil and calcareous clay, clayey nannofossil ooze, and clay/silty clay (Tables 2 and 3). Lighter shades of brown correspond to higher carbonate contents. Localized concentrations of Fe-rich dark yellowish brown (10YR 4/1) silt or silty clay occur throughout the Subunit. Bioturbation is moderate to intense, with faint irregular mottling; however, no identifiable trace fossils were observed.

Subunit IIB

Subunit IIB is characterized by an alternation of clay- and carbonate-rich lithologies on a variety of scales. These lithologies are locally mixed by moderate to intense bioturbation. Thin-to-medium thickness, generally upward-darkening color banding in shades of greenish gray is present throughout.

Major lithologies in Subunit IIB are olive-gray silty claystone or clayey siltstone and light greenish nannofossil or calcareous claystone. Minor lithologies include claystone, calcareous fine sandstones to siltstones, and silty nannofossil claystone. White nannofossil/foraminiferal chalk forms about 1% of the total thickness of Subunit IIB. In sandy and silty lithologies, biogenic silica (diatoms, sponge spicules, and radiolarians) is common (up to 5%-15% by volume). Grayish red purple (5RP4/2) and dusky blue (5PB 3/2) laminae or blebs (possibly manganese oxide) are scattered throughout.

The typical sequence of lithologies in Subunit IIB begins with a basal irregular thin bed (up to 5 cm thick, but more commonly 0.5-3 cm thick) of mixed biogenic (calcareous and siliceous) and terrigenous fine sandstone to siltstone (Fig. 13). Parallel lamination, cross lamination, ripple cross lamination (sometimes with flasers), and subtle, normally graded bedding are frequent in carbonate-rich sandstones

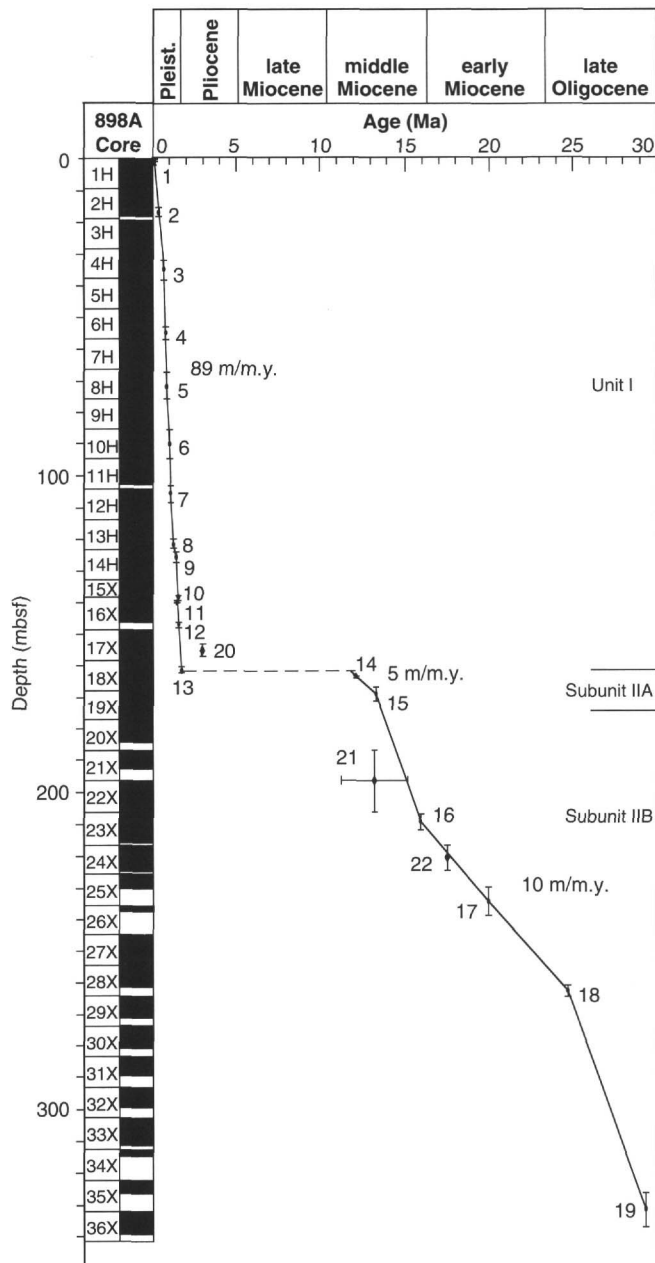


Figure 8. Depth vs. age curve for Site 898, plotted from data in Table 4 (see "Biostratigraphy" section, this chapter). Each data point is shown with depth and/or age error bars. Horizontal line is an unconformity. Light horizontal lines are major lithostratigraphic unit boundaries. Slopes of lines connecting adjacent data points are accumulation rates for that time or depth interval. Note that accumulation rates of lithostratigraphic Unit II are substantially lower than those of Unit I. Numbers refer to cores in Table 4.

and siltstones. Foraminifer-rich fine sandstones also show scattered, subtle, reversely-graded bedding, with concentrations of large foraminifer tests on bed tops.

The fine sandstone beds have sharp and flat bases and sharp to gradational tops (Fig. 14). Where tops are gradational, the transition from fine calcareous sandstone to the overlying nannofossil claystone is characterized by wavy, parallel, or lenticular alternating laminae of both lithologies, as well as by burrow mottling (Fig. 14). These sandy or silty beds make up about 5% of the total thickness of Subunit IIB.

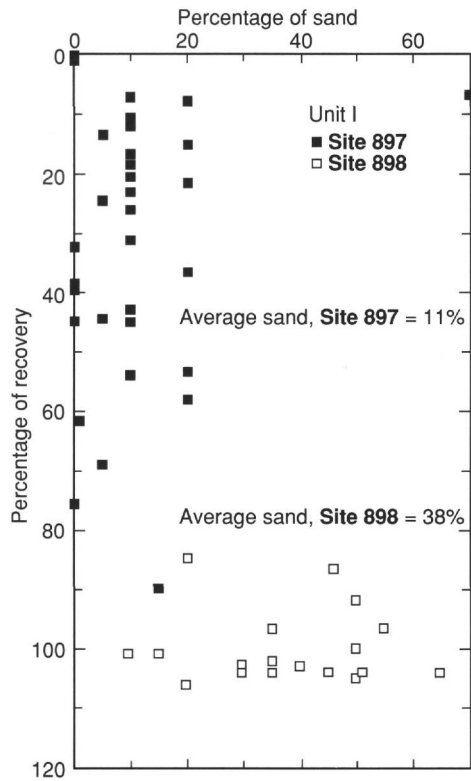


Figure 9. Core recovery vs. percentage of sand and silt in Units I at Sites 897 and 898.

This basal silt- and sand-rich lithology is overlain by color-banded (8-15 cm thick) clay-rich lithologies. Color variations correspond strongly to variations in the carbonate content (mostly nannofossils). Light-colored nannofossil claystones to clayey nannofossil chalks having varying contents of silt occur near the bases of the upward-darkening sequences. Darker colors correspond to the overlying silty claystones and claystones. The boundaries of colored bands have been locally disturbed by pervasive bioturbation.

Burrows are concentrated (or more clearly visible) in the light-colored, carbonate-rich lithologies in the lower part of each individual sequence. In places, intensive burrowing has modified the original depositional contacts within a sequence and, usually, the burrowing extends down the sequence to the basal calcareous sand bed. The most common trace fossils are *Planolites*, and *Chondrites*, with less abundant and isolated *Zoophycos* and *Skolithos*.

In addition to the dominant upward-darkening sequences, upward-lightening sequences, and intensely bioturbated, sharp-based, white nannofossil chalk beds also are seen.

Petrography

Sand- and silt-sized detritus in Unit II includes components essentially similar to the assemblage observed in Unit I. Unit II also contains clay-rich lithologies that are similar to those in Unit I, except that the Type 2 (oriented, carbonate-poor) clay-rich lithologies are a more persistent and volumetrically significant part of the lithologic assemblage. Both claystone types are present in repeated interbeds and in various shades of browns and green grays.

Based on the petrographic similarities with lithologies at Site 897 and the geographic proximity of the sites, the dominant clay minerals in Unit II are probably similar to those in Unit I (i.e., illite and kaolinite with a lesser proportion of expandable clay).

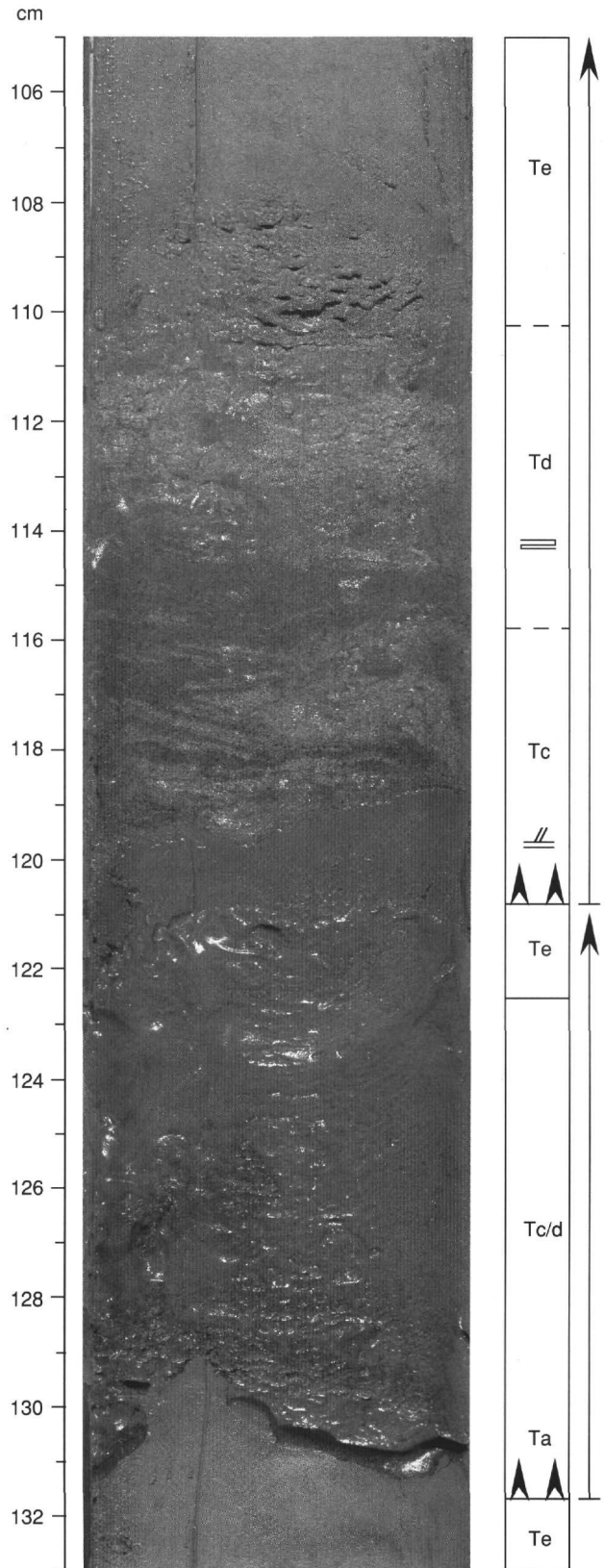


Figure 10. Two turbidites having sandy bases; the upper one contains small-scale cross-stratification and parallel lamination and has an erosional contact with the lower one. See caption for Figure 11 for key to letters (Unit I, Interval 149-398A-1H-6, 105-133 cm).

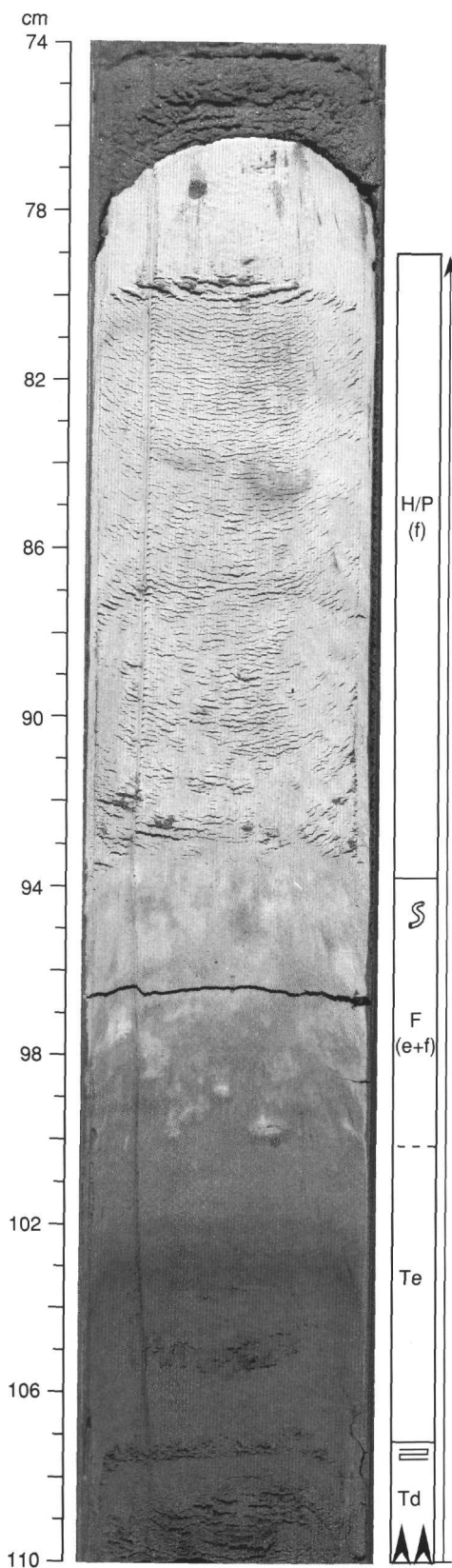


Figure 11. A turbidite sequence showing Bouma units Td and Te at the base. F = transitional terrigenous-carbonate interval mixed by bioturbation (Bouma units Te and f); H/P = hemipelagic and pelagic sediments (nannofossil ooze in this example); Bouma unit Tf (Unit I, Interval 149-898A-64R-4, 74-110 cm).

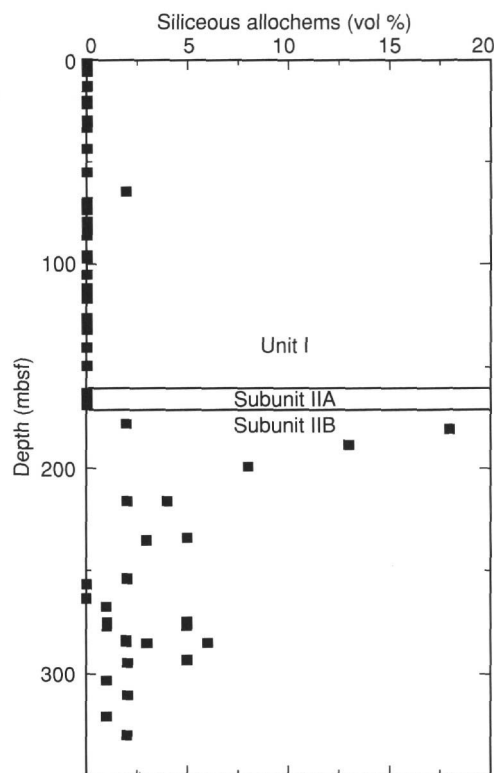


Figure 12. Content of siliceous allochems (diatoms, radiolarians, and siliceous sponge spicules) in dominant lithologies at Site 898. Data represent volume percent of these constituents in dominant lithologies, determined by visual estimate in smear slides.

Depositional Processes

Subunit IIA

The homogeneous lithologies in Subunit IIA are interpreted as a pelagic and hemipelagic facies. Depositional processes inferred for these facies include continuous, slow accumulation by settling through the water column and the absence of turbidity or other bottom currents.

Ubiquitous bioturbation in the sediments of Subunit IIA suggests deposition under conditions of normal oxidation. The relatively high content of biogenic carbonate indicates that deposition probably took place above the CCD. The position of the Subunit, sandwiched between the terrigenous sandy turbidites of Unit I and the distal, muddy, current-deposited facies of Subunit IIB, suggests deposition in an abyssal plain setting.

Subunit IIB

In Subunit IIB, upward-darkening alternations of carbonate-rich and relatively carbonate-poor sediments containing biogenic siliceous material contrast with the clearly turbidite-related lithologic association so characteristic of Unit I. Thin silty sand and silt intervals at the bases of many of the upward-darkening sequences lack the clear normal grading typical of turbidites. Many of these silty sands and silts contain small-scale cross stratification and parallel lamination, which indicates current activity (Figs. 13-15). Some exhibit inverse grading or have sharp tops as well as sharp bases and are overlain by "lag deposits" of large foraminifers. All these features point to reworking by contour currents, as described by Stow and Piper (1984). It is possible that some of the homogeneous, carbonate-poor terrigenous silty claystones and claystones are mud turbidites. In general, the ubiquitous presence of minor pelagic intervals (nannofossil claystone

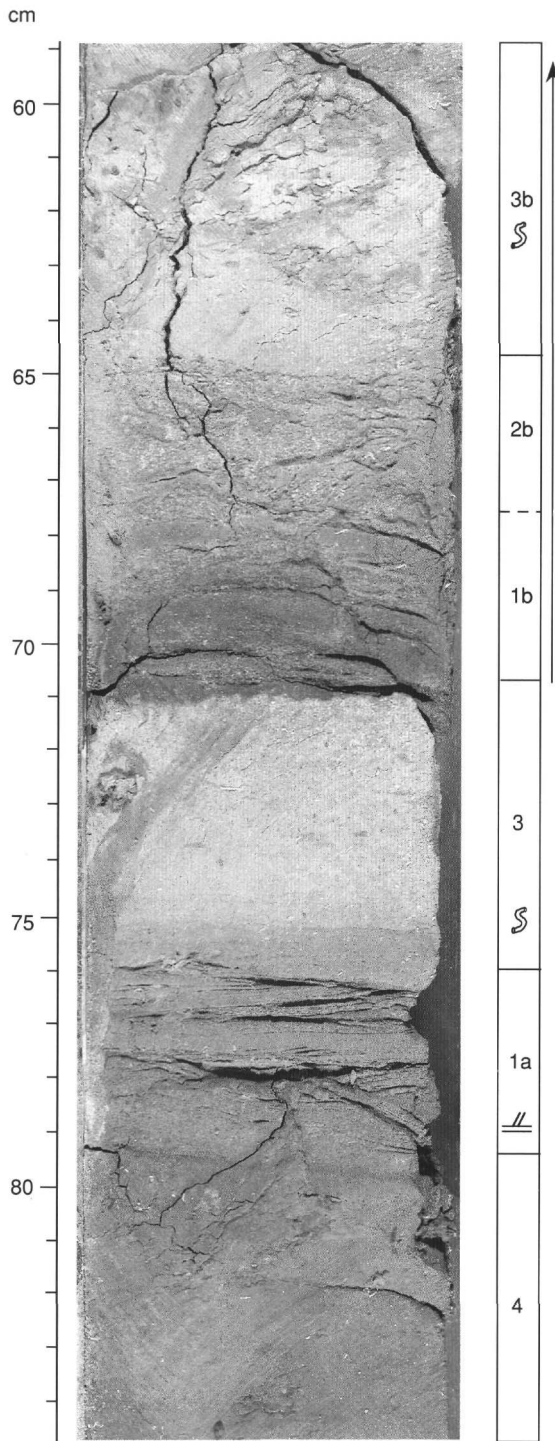


Figure 13. Example of irregular vertical variation within individual sequences. An upper, normally graded laminated sequence is interpreted as a muddy turbidite, with parallel-laminated sandy siltstone and silty claystone at its base (1B), grading upward to silty claystone (2B) and light-colored bioturbated claystone with silt (3B). Lower sequence shows cross-stratified and parallel-laminated, mixed biogenic and terrigenous sandstone (1A), with a sharp base and top intercalated between structureless, light-colored nanofossil clay (3) and darker silty clay (4); 1A is interpreted as a contourite (Subunit IIB, Interval 149-898A-33X-3, 59-84 cm).

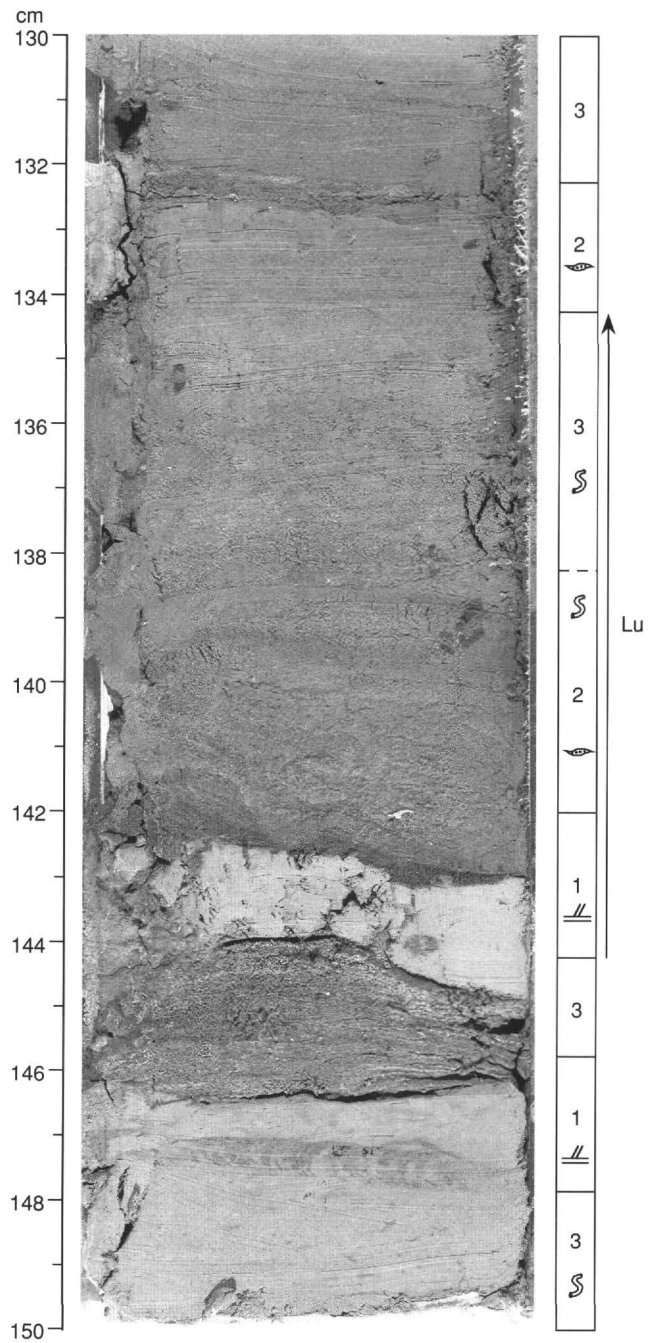


Figure 14. Massive or poorly laminated, sharp-based fine sandstone (1) occurs beneath a bioturbated, positively graded and upward-lightening sequence (Lu). The transition from sandstone bed to bioturbated nanofossil claystone at the top (3) takes place through an interval of bioturbated nanofossil claystone having lenses and mottles of silt (2); a similar interval occurs at 132.5 cm. Note horizontal *Zoophycos* (at 148 cm) in nanofossil clay (3) and overlying sandstone with sharp base and top. These sequences have been interpreted as contourite deposits (Subunit IIB, Interval 149-898A-33X-5, 130-150 cm).

to nanofossil chalk) suggests that deposition of Subunit IIB occurred above the CCD.

The combination of possible turbidites and contourites observed in this Subunit is not unexpected. Possible biostratigraphic hiatuses (see "Biostratigraphy" section, this chapter), relatively low sediment accumulation rate, and the physiography of the Cenozoic Iberian

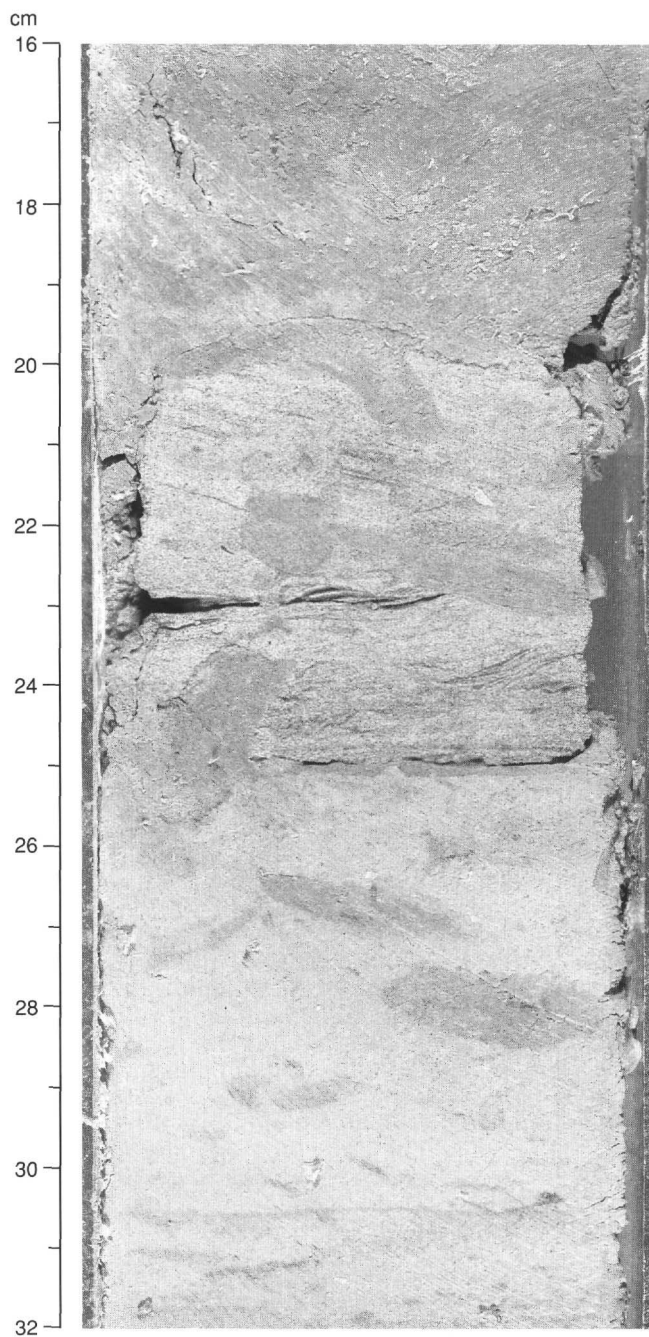


Figure 15. Bioturbated and cross-laminated calcareous, mixed terrigenous and biogenic fine sand layer (1) intercalated between bioturbated dark silty claystone (4) at top and bioturbated nanofossil clay at bottom (3). Note the sharp top and base of the sandy bed and burrows cutting across lithological boundaries. This interval is interpreted as a contourite deposit (Subunit IIB, Interval 149-898A-22X-1, 16-32 cm).

margin are all factors consistent with contourite development (see Comas and Maldonado, 1988).

BIOSTRATIGRAPHY

Sediments recovered from the two holes cored at Site 898 provide a discontinuous record for the Pleistocene through the upper Oligocene. Calcareous nannofossils generally are abundant to very abundant in all of the sedimentary sequence. Planktonic and benthic foraminifers

are abundant to common in the top 157 m of Hole 898A, but are mostly less common below that depth.

Calcareous Nannofossils

Site 898 is located in the eastern part of the Iberia Abyssal Plain (water depth of 5278 m). Hole 898A was cored to a depth of 341.5 mbsf, with a total recovery of 289.22 m of sediment. On the basis of the calcareous nannofossils, we defined two stratigraphic successions, one from the upper Pleistocene (Zone NN21 of Martini, 1971) to the uppermost Pliocene (Zone NN19) and the other from the middle Miocene (Zone NN7) to the upper Oligocene (Zone NP24). A major hiatus representing most of the Pliocene to the upper Miocene lies within Core 149-898A-18X; this also corresponds to the transition from lithostratigraphic Unit I to Subunit IIA (Section 149-898A-18X-4 at 75 cm; see "Lithostratigraphy" section, this chapter). Most of the material in Unit I was deposited by turbidity currents. To eliminate the influence of reworked specimens, biostratigraphic age assignments were determined by one or more samples from the pelagic intervals in every core. The nannofossil record indicates that the Pliocene/Pleistocene boundary is at the top of Core 149-898A-17X.

Calcareous nannofossils generally are very abundant and well-preserved in the Pleistocene through the latest Pliocene age interval (0-162.34 mbsf), but become less abundant and moderately to well-preserved in the middle Miocene through the upper Oligocene age interval. The biostratigraphy for Site 898 is summarized in Figure 16.

Sample 149-898A-1H-1, 7 cm, contains rare specimens of *Emiliania huxleyi* and *Emiliania pujosae*, but no *Pseudoemiliania lacunosa* and has been assigned to Zone NN21 from the uppermost Pleistocene. This sample is older than 85 k.y., as indicated by the dominance of small *Gephyrocapsa* spp. (>2.5 μm) having an open central area (morphogroup 1 of Gard and Backmann, 1990). Samples 149-898A-1R-1, 80 cm, and -2R-6, 106 cm, belong to Zone NN20, as indicated by the absence of *Emiliania huxleyi* and *Pseudoemiliania lacunosa*. Sample 149-898A-1R-1, 80 cm, has abundant *Gephyrocapsa* spp. (>2.5 μm) having an open central area; abundant *Gephyrocapsa* spp. (<2.5 μm ; morphogroups 1 and 2 of Gard and Backmann, 1990); and few *Gephyrocapsa* spp. (>2.5 μm) having a closed central area (morphogroup 3). Sample 149-898A-2R-6, 106 cm, contains abundant *Gephyrocapsa* spp. (>2.5 μm) having both open and closed central areas (morphogroups 1 and 3). The interval from Sample 149-898A-2H-CC to -18X-4, 75 cm, was assigned to Zone NN19.

To improve the zonal scheme for Site 898, the subzones defined by Rio et al. (1990) were integrated into Figure 16 (Subzones NN19A-NN19F). Very abundant small *Gephyrocapsa* spp. (>2.5 μm) having an open central area, common small *Gephyrocapsa* spp. (>2.5 μm) having a closed central area, and very rare *Pseudoemiliania lacunosa* occur in Sample 149-898A-2H-CC; these indicate the top of Subzone NN19F. The highest occurrence (HO) of *Reticulofenestra* sp. A (>6.5 μm) was recognized in Sample 149-898A-4H-CC. The lowest occurrence (LO) of *Gephyrocapsa omega* (>4.0 μm) can be seen in Sample 149-898A-6H-4, 77 cm; it indicates the top of Subzone NN19E. The LO of *Reticulofenestra* sp. A (>6.5 μm) was recorded in Sample 149-898A-8H-1, 78 cm. Sample 149-898A-10H-CC contains the HO of *Gephyrocapsa caribbeanica* (>5.5 μm) and very rare *Helicosphaera sellii*; it corresponds to the top of Subzone NN19D (1.10-1.12 Ma). The consistent occurrence of *Helicosphaera sellii* from Sample 149-898A-12H-3, 104 cm, was used to determine the top of Subzone NN19C (1.20 Ma). The LO of *Gephyrocapsa caribbeanica* (>5.5 μm), was seen in Sample 149-898A-13H-4, 134 cm. The HO of *Calcidiscus macintyreii* (circular, >10.0 μm ; in Sample 149-898A-15X-CC) marked the top of Subzone NN19B. The LO of *Gephyrocapsa oceanica* (>4.0-5.0 μm = *Gephyrocapsa oceanica* s.l.) can be seen in Sample 149-898A-16X-1, 59 cm. The LO of *Gephyrocapsa caribbeanica* (>4.0 μm), in Sample 149-898A-16X-CC, indicated the top of Subzone NN19A (1.64 Ma) and also the location of the Pliocene/Pleistocene boundary (1.65 Ma). Intervals 149-898A-17X-1, 12

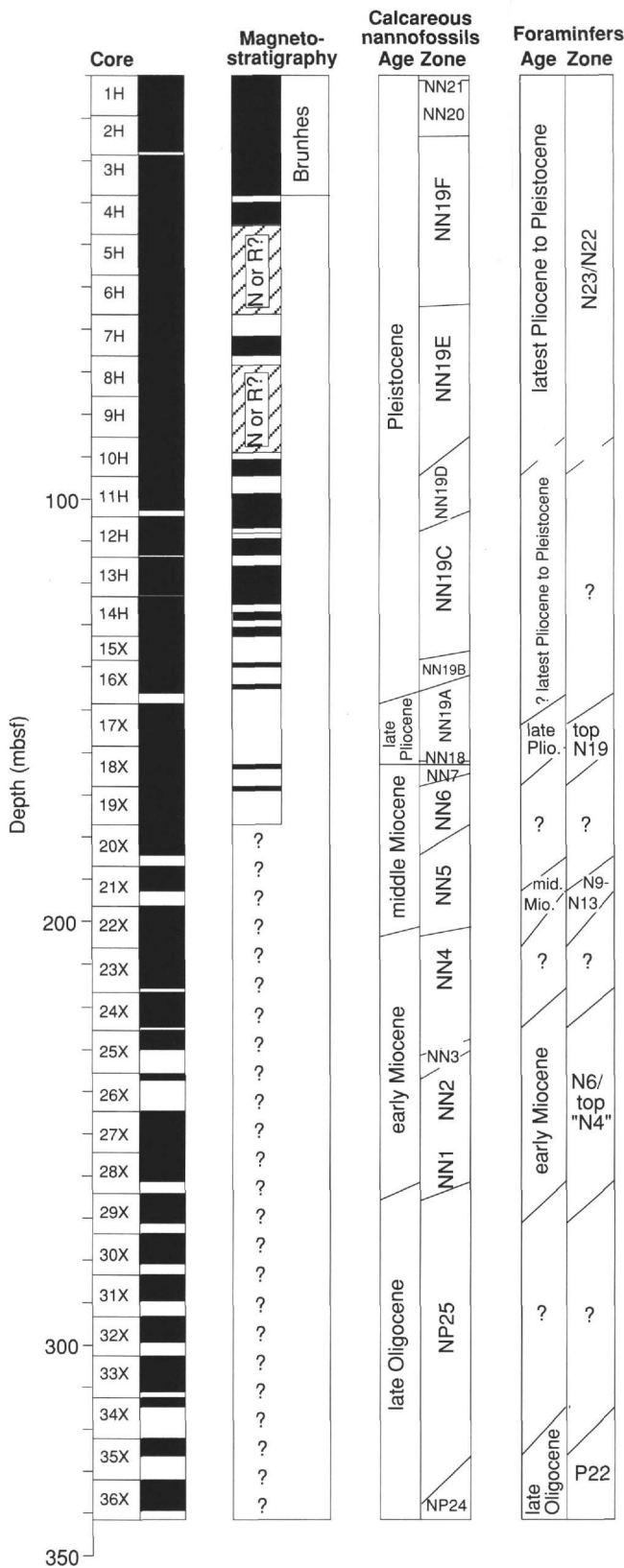


Figure 16. Summary of magnetostratigraphy and planktonic microfossil zones from Site 898.

cm, and 149-898A-18X-3, 56 cm, were assigned to the uppermost Pliocene Subzone NN19A on the basis of the absence of *Discoaster* spp. and *Gephyrocapsa caribbeanica* (>4.0 µm). Sample 149-898A-18X-4, 58 cm, contains abundant *Coccolithus doronocoides*, rare *Gephyrocapsa* spp. (small), rare *Discoaster brouweri brouweri*, very rare *Discoaster brouweri triradiatus*, and *Discoaster variabilis*. This assemblage places this sample within the upper Pliocene Zone NN18.

Intervals 149-898A-18X-4, 134 cm, to -18X-5, 5 cm, contain *Discoaster kugleri* and *Coccolithus miopelagicus* and lacks *Catinaster coalitus* and *Cyclicargolithus floridanus*. This assemblage indicates a middle Miocene age (Zone NN7). The HO of *Cyclicargolithus floridanus* and *Coronocyclus nitescens* and the absence of *Discoaster kugleri* in Sample 149-898A-18X-CC indicate Zone NN6. Sample 149-898A-19X-3, 140 cm, contains *Sphenolithus heteromorphus* and defines the top of Zone NN5. The LO of *Calcidiscus macintyreii* is recorded in Sample 149-898A-21X-1, 8 cm. *Helicosphaera ampliaperta*, in Sample 149-898A-22X-4, 107 cm, indicates the top of Zone NN4, whereas the LO of *Calcidiscus leptoporus*, in Sample 149-898A-25X-3, 35 cm, indicates the base of Zone NN4. In Sample 149-898A-26X-2, 63 cm, few *Triquetrorhabdulus carinatus*, common *Helicosphaera scissura*, very rare *Helicosphaera recta*, and the absence of *Helicosphaera ampliaperta* and *Cyclicargolithus abisectus* indicate Zone NN2. In Sample 149-898A-27X-4, 107 cm, few *Zygrhablithus bijugatus* and *Triquetrorhabdulus carinatus*, very rare *Cyclicargolithus abisectus*, *Reticulofenestra bisecta*, *Sphenolithus ciperoensis* and *Discoaster woodringii*, and common *Clausicoccus fenestratus* indicate the lowermost Miocene Zone NN1. Sample 149-898A-28X-CC has very rare *Cyclicargolithus abisectus*, *Reticulofenestra bisecta*, rare *Zygrhablithus bijugatus*, and common *Clausicoccus fenestratus*. Intervals 149-898A-29X-1, 45 cm, to -35X-CC were assigned to the uppermost Oligocene Zone NP25. The common occurrence of *Cyclicargolithus abisectus* and *Reticulofenestra bisecta* and the presence of *Pontosphaera enormis* in Sample 149-898A-29X-1, 45 cm, are used to determine the top of Zone NP25 and, thus, the Oligocene/Miocene boundary. The LO of *Triquetrorhabdulus carinatus* and the HO of *Sphenolithus distentus* can be seen in Sample 149-898A-32X-CC. Sample 149-898A-35X-CC contains abundant *Cyclicargolithus abisectus*, common *Helicosphaera recta* and *Reticulofenestra bisecta*, few *Sphenolithus ciperoensis*, rare *Sphenolithus distentus*, and very rare *Chiasmolithus altus*. Sample 149-898A-34X-CC contains few *Sphenolithus ciperoensis*, rare *Sphenolithus distentus*, and very rare *Sphenolithus predistentus*. Intervals 149-898A-36X-4, 90 cm, to -36X-CC contain few *Helicosphaera compacta* and *Sphenolithus distentus*, rare *Chiasmolithus altus*, and lacks *Sphenolithus ciperoensis*. This assemblage indicates Zone NP24.

Hole 898B

One core was recovered from Hole 898B. Sample 149-898B-1H-3, 149 cm, has very abundant, well-preserved calcareous nannofossils. The assemblage has very abundant small *Gephyrocapsa* spp. (>2.5 µm) having an open central area (morphogroup 1 of Gard and Backmann, 1990), but lacks *Emiliania huxleyi* and *Pseudoemiliania lacunosa* and was assigned to Zone NN20 from the uppermost Pleistocene. Sample 149-898B-1H-CC contains few, poorly preserved calcareous nannofossils. The low diversity of this assemblage does not allow for a precise age assignment.

Foraminifers

Planktonic foraminifers in core-catcher samples from Holes 898A and 898B were examined to establish preliminary ages for the sediments. Samples from the upper sections of Hole 898A contained a moderately diverse planktonic foraminiferal assemblage having good to moderate preservation. Samples from the lower intervals of Hole 898A contained a less diverse planktonic foraminiferal assemblage

(Table 5). Similar patterns were observed in the benthic foraminiferal assemblages.

Holes 898A and 898B

A late Pliocene to Pleistocene age sequence (Zones N22-N23) was identified in Intervals 149-898A-1H-CC to -9H-CC. These samples are characterized by the co-occurrence of *Globorotalia tosaensis* and *Globorotalia truncatulinoides*. *Globigerinoides extremus*, which is usually used as a marker for the base of Zone N22, is present at the top, and is scattered within, this interval. These occurrences were interpreted as having been reworked into the upper part of Zones N22 and N23, taking into consideration the younger nannofossil zones and ages in the upper part of this interval. Abyssal and reworked shallow-water benthic foraminifers were identified throughout this interval. Sample 149-898B-1H-CC also belongs in Zones N22 to N23.

Intervals 149-898A-10H-CC to -16X-CC are characterized by the absence of *Globorotalia truncatulinoides* and the rare occurrence of *Globorotalia tosaensis*. Although the absence of *Globorotalia truncatulinoides* suggests that this interval may be assigned to Zone N21, which is of late Pliocene age, we have not assigned this age to the assemblage, because of the absence of other zonal markers as well. Calcareous nannofossil evidence does not support a late Pliocene age; nannofossil zonal markers restricted to the early Pleistocene have been found in this interval. The discrepancy in age dating may be the result of mass transport of upper Pliocene sediments into lower Pleistocene sediments, which were barren of planktonic foraminifers, or at least the zonal markers.

Changes in the characteristics of the water mass may also account for the absence of *Globorotalia truncatulinoides* and the rare occurrence of *Globorotalia tosaensis* in this interval. Both of these species are warm subtropical to tropical species and are rare in temperate regions (Kennett and Srinivasan, 1983). The relatively common presence of cooler water species, such as *Neogloboquadrina pachyderma*, indicates sedimentation under cool-water conditions and also may explain the absence of *Globorotalia truncatulinoides*. Additional analysis of hemipelagic Samples 149-898A-14H-3, 98-99 cm; -15X-2, 45-47 cm; -16X-1, 59-61 cm; and -17X-4, 108-110 cm, did not yield any specimens of *Globorotalia truncatulinoides*.

Sample 149-898A-17X-CC contains *Globorotalia tosaensis* and *Globorotalia inflata* and can be assigned to the upper part of Zone N19, which is of late early to early late Pliocene age. Additional analysis of Sample 149-898A-17X-4, 108-110 cm, yielded *Sphaeroidinellopsis paenedehiscens*, *Globorotalia tosaensis*, *Globorotalia inflata*, and *Neogloboquadrina atlantic*, allowing us to assign it to the top of Zone N19. Samples 149-898A-18X-CC, -19X-CC, and -20X-CC contain no zonal markers.

If, on the basis of calcareous nannofossils, the Pliocene/Pleistocene boundary is just below Sample 149-898A-16X-CC, then planktonic foraminiferal evidence indicates that a hiatus occurs between this and Sample 149-898A-17X-4, 108-110 cm, where Zone N21 is missing. The planktonic foraminifer assemblage suggests an age of early late Pliocene for Sample 149-898A-17X-CC, which conflicts with the calcareous nannofossil age of latest Pliocene for the same sample.

Sample 149-898A-21X-CC contains *Cassigerinella chipolensis*, *Neogloboquadrina mayeri*, and *Sphaeroidinellopsis disjuncta*, while *Globigerina nepenthes* is absent. This sample can be assigned to Zones N9 to N13, which indicates a middle Miocene age. This sample also contains *Globorotalia* sp. 1 of Iaccarino and Salvatorini (1979), which was recorded in lower Miocene sediments at DSDP Site 398. Samples 149-898A-22X-CC and -23X-CC are barren.

Intervals 149-898A-24X-CC to -28X-CC are characterized by the presence of *Catapsydrax dissimilis* at the top and *Globoquadrina dehiscens* at the base. The interval can be assigned to the top of Zones "N4" to N6, which are of early Miocene age. No zonal marker species were present in Samples 149-898A-29X-CC, -30X-CC, -31X-CC, -32X-CC, -33X-CC, and -34X-CC.

Samples 149-898A-35X-CC and -36X-CC contain *Globigerina angulisuaturalis* and *Globigerina ciperoensis*. This interval can be assigned to the lower part of Zone P22, which is of late Oligocene age.

PALEOMAGNETISM

Magnetic measurements, using the pass-through cryogenic magnetometer, were made on all archive halves of cores recovered from Hole 898A. Alternating field (AF) demagnetization of these archive halves was performed at 10-cm intervals using a peak field intensity of 15 mT. Cores 149-898A-4H through -14H (with the exception of Core 149-898A-12H, whose data were lost because of failure of a multishot tool) were oriented in situ using the tensor orientation tool (see "Explanatory Notes" chapter, this volume). Twenty-one discrete samples taken from the working halves of cores were progressively AF demagnetized and measured with the cryogenic magnetometer. The magnetic susceptibility of all cores was routinely measured at intervals of 3 cm on the Multisensor Track.

Magnetostratigraphy

The majority of the whole-core pass-through measurements were of high quality and agree well with the discrete sample data. The mean inclination value is close to the expected inclination (59.7°) at the site from the Pleistocene to the present. In contrast to the overall excellence of the pass-through measurements obtained from APC cores, data from the XCB cores were less satisfactory. The NRM intensities for Cores 149-898A-20X through -36X are weak, and the data are highly scattered. Therefore, polarity interpretations for these cores were not attempted on board. The main features of our tentative magnetostratigraphic interpretation of the remaining cores at Site 898 are summarized in Figure 17. This interpretation is based on preliminary biostratigraphic ages (see Fig. 16 in "Biostratigraphy" section, this chapter).

The magnetic behavior of Cores 149-898A-1H through -3H is similar to that of their counterparts at Hole 897A. The stable component of remanent magnetization for all these cores is normal polarity. Declinations vary substantially within some individual sections of these cores, even after orientation using the tensor tool data. This indicates either an incomplete removal of the secondary magnetization, or rotation of the recovered material within the core liner or a combination of both. Biostratigraphic ages in these cores range from 0.3 to 0.8 Ma. Thus, in conjunction with the biostratigraphic data, we can assign these cores to the Brunhes Chron (<0.78 Ma).

The first evidence for a polarity reversal was found in Core 149-898A-4H at a depth of 28.2 mbsf (confirmed by a discrete sample measurement and by changes of about 180° in declination between normal and reversed intervals; Fig. 17). Thus, this magnetic polarity shift from normal to reversed may represent the Brunhes/Matuyama boundary (0.78 Ma). However, the next distinctive reversal did not occur until Core 149-898A-7H at 57.0 mbsf. The failure to reveal more reversed magnetizations from cores recovered from the interval (28.2-57.0 mbsf, i.e., a period of expected reversed polarity) may have resulted from an unrecognized sedimentary hiatus or from a large magnetic normal overprint during the Brunhes Chron. Preliminary planktonic foraminiferal dates suggest that sediments below a depth of 85.0 mbsf are of late Pliocene age. This information would suggest that the shift of polarity from reversed to normal at about 92.0 mbsf should correspond to the upper Olduvai boundary. However, the correlation of the three normal polarity intervals (63.0-66.0 mbsf, 98.0-107.0 mbsf, and a very short one at 107.0 mbsf) with Cobb Mountain, Reunion, and an excursion within the Matuyama Chron, respectively, is questionable (Fig 17).

Pass-through cryogenic magnetometer measurements identified several magnetic reversals from 94.7 to 215.6 mbsf. Large uncertainty in the interpretation of key foraminiferal and nannofossil biostratigraphic markers (see Fig. 16 in "Biostratigraphy" section, this chapter) at this time do not permit a tentative correlation of these polarity

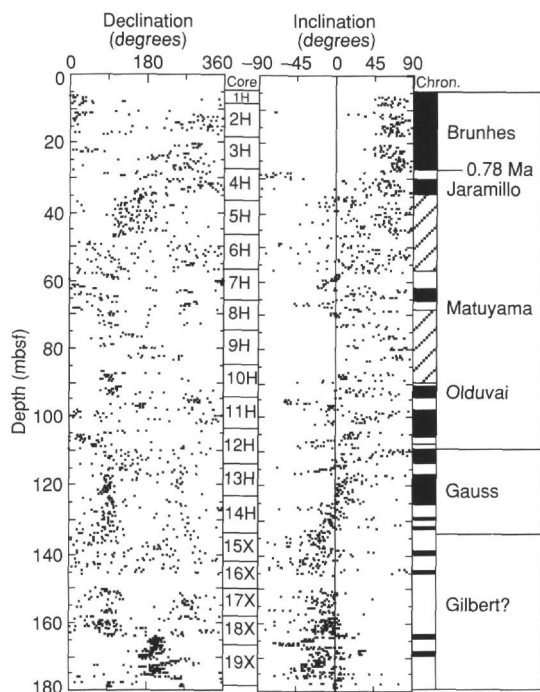


Figure 17. Magnetic inclination and declination for Cores 149-898A-1H to -20X in Hole 898A (after AF demagnetization at 15 mT). Tentative interpretation of the magnetostratigraphy is shown on the right; zones in black (white) correspond to normal (reversed) polarity; shaded areas represent uncertain polarity intervals.

intervals with the geomagnetic time scale. However, we noticed that the inclinations are dominantly normal between 110.0 to 133.0 mbsf, suggesting that this interval may correspond to a period of predominantly normal polarity.

Cryogenic magnetometer measurements also suggest several polarity reversals, which were recorded in Cores 149-898A-20X through -36X (177.4-339.7 mbsf). These polarity signals may not be reliable because of the weak magnetization of most of the sediments from 216.4 to 339.7 mbsf. We have not calibrated the measurements using corresponding discrete samples. Detailed studies of discrete samples and more accurate biostratigraphic markers will be needed to constrain a more reliable correlation of these intervals with the geomagnetic reversal time-scale.

Magnetic Susceptibility

Figure 18 shows the downhole profile of magnetic susceptibility for Hole 898A. Within the top 150 m, the magnetic susceptibilities have values that are consistently about 3×10^{-4} SI units. These relatively high susceptibility values correspond to Unit I (see "Lithostratigraphy" section, this chapter). The greatest susceptibility maximum occurs at about 98 mbsf. An examination of the corresponding core photograph reveals an interval of dark-colored soupy sand at the base of a turbidite sequence. Similar to Site 897, the high and low susceptibility peaks shown in Figure 18 generally correlate well with the turbidite layering. Lows correspond to the pelagic clays at the top of turbidite sequences and highs correspond to the terrigenous sands at the base of turbidite sequences. The susceptibility values decrease below about 163 mbsf (to about 1×10^{-4} SI units) in the pelagic sediments from Cores 149-898A-18X to -36X of Unit II. The low susceptibility values, the weak NRM intensities, as well as the relatively high percentage of quartz and feldspar observed in smear-slides from these cores, suggest that there are only minor amounts of magnetic material in these sediments.

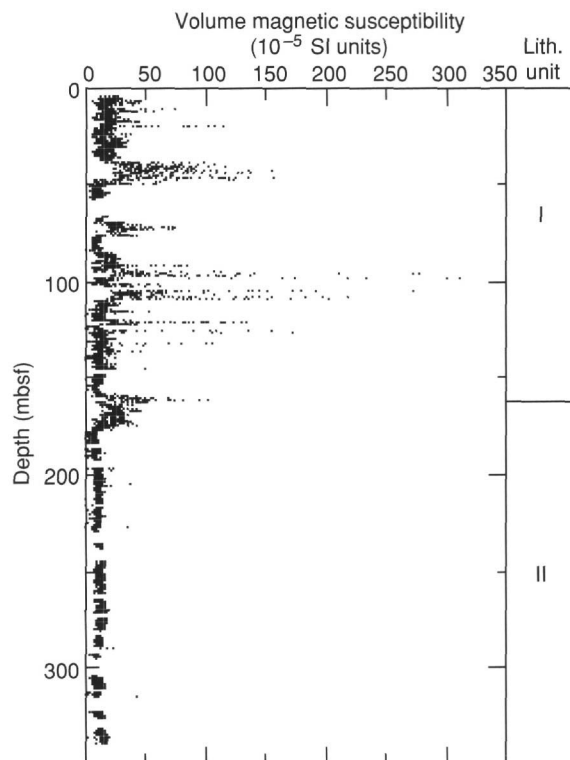


Figure 18. Downhole profile of magnetic susceptibility in Hole 898A.

ORGANIC GEOCHEMISTRY

Concentrations of calcium carbonate and organic carbon were measured in samples obtained regularly from Holes 898 A and 898B. Organic matter atomic C/N ratios and Rock-Eval pyrolysis results were employed to determine the type of organic matter contained within the sediments. Routine monitoring of headspace gas contents, done for drilling safety, yielded interesting information about the formation and migration of biogenic methane in these passive margin sediments.

Concentrations of Inorganic and Organic Carbon

Concentrations of carbonate carbon vary between a high of 9.6% to essentially zero in sediments from Site 898 (Table 6). These carbonate carbon concentrations are equivalent to 80% to 0% CaCO_3 in the sediments, assuming that all of the carbonate is present as pure calcite. The variability in carbonate content reflects a history of generally low biological productivity and deposition of hemipelagic sediments below the CCD, combined with delivery of carbonate-rich turbiditic sediments that initially had been deposited in shallower waters.

Concentrations of organic carbon are relatively elevated in the upper part of the Site 898 lithologic column (Table 6). Lithologic Unit I, a Pleistocene to lower Pliocene turbidite-containing sequence, averages nearly 0.5% organic carbon (Fig. 19). This average is significantly greater than the average of 0.2% calculated from DSDP Legs 1 through 31 by McIver (1975). The two principal sources of organic matter in oceanic sediments are from production of marine algal and land plant detritus supplied by rivers and winds. Algal organic matter typically is oxidized and largely recycled during, and shortly after, settling to the seafloor (e.g., Suess, 1980; Emerson and Hedges, 1988). The land-derived organic matter that is delivered to deep-sea sediments is generally the less-reactive material that survives transport to the ocean. Consequently, the elevated concentrations of organic carbon found in lithologic Unit I result from special

Table 6. Concentrations of total, inorganic, and organic carbon in sediments and rocks from Holes 898A and 898B.

Core, section, interval (cm)	Depth (mbsf)	Total C (%)	Inorg. C (%)	Org. C (%)	CaCO ₃ (%)	Org. C/N	Org. C/S	Lithologic unit
149-898B-1H-1, 22-24	0.22	5.66	5.39	0.27	45	9.0	13.0	Unit I: silty clay, silt, and fine sand
149-898A-1H-3, 67-68	3.67	2.38	2.22	0.16	19	4.0	2.3	
1H-5, 43-44	6.43	6.93	6.48	0.45	54	22.0		
1H-5, 133-134	7.33	7.82	7.64	0.18	64			
2H-3, 42-43	12.62	3.37	3.03	0.34	25	8.5	8.5	
2H-4, 58-59	14.28	5.12	4.39	0.73	37	12.0	14.0	
3H-2, 106-108	21.26	8.82	8.78	0.04	73		4.0	
3H-3, 52-63	22.24	6.71	6.54	0.17	55			
3H-4, 9-10	23.31	9.88	9.51	0.37	79	9.2		
4H-2, 53-54	30.23	1.43	1.05	0.38	9	4.7		
4H-2, 78-79	30.48	4.70	4.26	0.44	36	8.8		
4H-2, 131-132	31.01	4.73	4.60	0.13	38	1.4	6.5	
4H-5, 91-92	35.11	7.29	7.06	0.23	59			
5H-4, 108-109	43.31	0.58	0.35	0.23	3	3.3		
5H-5, 86-87	44.59	2.03	1.72	0.31	14	6.2	1.8	
6H-4, 77-78	52.48	7.45	7.34	0.11	61	3.6	1.2	
6H-6, 63-64	55.35	3.99	3.47	0.52	29	7.4	3.7	
6H-6, 77-78	55.49	3.19	2.54	0.65	21		2.9	
6H-6, 92-93	55.64	0.97	0.82	0.15	7	7.5	0.9	
7H-4, 79-80	61.99	2.75	1.67	1.08	14	12.0	2.8	
7H-6, 63-64	64.83	3.39	2.65	0.74	22	15.0	0.9	
7H-6, 79-80	64.99	2.60	2.17	0.43	18	21.0	0.5	
7H-6, 93-94	65.13	8.64	8.58	0.06	72		0.7	
8H-1, 103-104	67.23	3.46	3.07	0.39	26	3.9		
8H-5, 106-107	73.32	0.82	0.49	0.33	4	3.6	2.7	
8H-7, 60-61	75.86	1.25	0.90	0.35	8	11.0	4.4	
9H-4, 24-25	80.55	4.03	2.26	1.77	19	22.1	2.0	
9H-6, 97-98	84.28	3.81	3.56	0.25	30	8.3	2.1	
10H-3, 85-86	89.05	3.36	2.94	0.42	25	6.0	6.0	
10H-5, 81-82	92.01	2.73	1.88	0.85	16		3.8	
11H-1, 106-107	95.76	1.47	0.94	0.53	8	7.6		
11H-2, 73-74	96.95	0.43	0.27	0.16	2		16.0	
11H-5, 26-27	100.98	7.33	6.93	0.40	58	10.0		
12H-3, 105-106	108.27	2.25	1.76	0.49	15	6.1	24.0	
13H-1, 89-90	114.59	7.21	7.01	0.20	58	6.6	20.0	
14H-3, 79-80	117.49	2.57	1.87	0.70	16	8.7		
13H-4, 27-28	118.47	6.90	6.86	0.04	57	0.4		
13H-6, 95-96	122.15	4.74	1.41	3.33	12	83.2		
14H-1, 148-149	124.68	9.15	9.01	0.14	75	1.3		
14H-3, 84-85	127.07	6.57	6.35	0.22	53	4.4	7.3	
14H-5, 74-75	130.00	4.03	3.73	0.30	31	2.5	5.0	
14H-5, 77-78	130.03	1.53	1.15	0.38	10	5.4	3.4	
15X-1, 45-46	133.15	2.36	1.97	0.39	16	6.5	39.0	
15X-2, 43-44	134.63	1.94	1.41	0.53	12	13.0	1.5	
15X-4, 109-110	138.29	9.66	9.60	0.06	80	0.5		
16X-1, 32-33	139.12	6.93	6.61	0.32	55	2.9		
17X-1, 70-71	149.20	2.45	1.85	0.60	15	10.0	0.2	
17X-2, 100-101	151.00	4.21	3.45	0.76	29	8.4	2.4	
17X-2, 134-135	151.34	7.37	7.27	0.10	61	0.8	10.0	
17X-6, 32-33	156.32	9.60	9.53	0.07	79	0.7		
18X-4, 144-145	164.06	0.70	0.69	0.01	6	0.1		Subunit IIA: silty clay and nannofossil clay.
18X-5, 22-23	164.34	1.25	1.21	0.04	10			
18X-5, 55-56	164.67	4.90	4.89	0.01	41	0.1		
18X-6, 80-81	166.42	3.20	3.18	0.02	27	0.2		
18X-CC, 4-5	167.61	7.23	7.22	0.01	60	0.1		
19X-1, 35-36	168.15	3.55	3.54	0.01	30	0.1		
19X-2, 83-84	170.13	0.40	0.39	0.01	3	0.1		
19X-3, 149-150	172.29	5.54	5.51	0.03	46	3.0		Subunit IIB: silty claystone and nannofossil claystone.
20X-3, 44-45	180.84	8.83	7.39	1.44	62			
21X-2, 3-4	188.53	7.36	7.12	0.24	59	12.0		
21X-2, 56-57	189.06	4.07	4.03	0.04	34	1.0		
21X-3, 20-21	190.20	5.28	5.26	0.02	44	2.0		
21X-3, 97-98	190.97	7.50	7.49	0.01	62	0.1		
22X-2, 64-65	198.84	4.91	4.96		41			
22X-3, 136-137	201.06	1.05	0.97	0.08	8	0.5	4.0	
22X-5, 87-88	203.57	5.14	5.09	0.05	42	0.5	1.0	
23X-1, 78-79	207.18	3.47	3.31	0.16	28	1.1	4.0	
23X-1, 89-90	207.29	0.31	0.25	0.06	2	0.4	1.0	
23X-4, 50-51	211.42	2.23	2.05	0.18	17	1.4	6.0	
23X-5, 60-61	213.02	1.66	1.37	0.29	11	2.6	0.5	
24X-1, 136-137	217.76	3.59	2.93	0.66	24	3.9	2.5	
24X-1, 137-138	217.77	1.59	1.45	0.14	12	1.0		
24X-2, 27-28	218.17		4.07		34			
24X-2, 30-31	218.20	1.05	0.65	0.40	5	2.5	5.0	
24X-4, 119-120	222.11	2.31	2.25	0.06	19	0.4		
25X-1, 60-61	226.20	0.35	0.24	0.11	2	0.9	2.2	
25X-1, 121-122	226.81	3.75	3.67	0.08	31	0.7	8.0	
25X-3, 39-40	229.02	2.56	2.47	0.09	21	0.8		
26X-1, 101-102	236.21	2.92	2.54	0.38	21	2.4		
26X-2, 20-21	236.90	2.74	2.68	0.06	22	0.5	2.0	
27X-1, 105-106	245.85	0.88	0.83	0.05	7	0.4		
27X-3, 82-83	248.62	3.21	3.13	0.08	26	0.7		
27X-3, 136-137	249.16	1.95	1.94	0.01	16	0.1		
27X-4, 105-106	250.37	4.62	4.57	0.05	38	0.4		
28X-1, 77-78	255.27	1.01	0.88	0.13	7	1.1		

Table 6 (continued).

Core, section, interval (cm)	Depth (mbsf)	Total C (%)	Inorg. C (%)	Org. C (%)	CaCO ₃ (%)	Org. C/N	Org. C/S	Lithologic unit
28X-1, 107-108	255.57	3.40	3.32	0.08	28	1.0		
28X-1, 133-134	255.83	0.29	0.19	0.10	2	1.6	1.2	
28X-2, 51-52	256.51	2.38	2.36	0.02	20	0.6		
28X-2, 88-89	256.88	3.60	3.30	0.30	28	7.5		
29X-2, 33-34	266.03	0.24	0.20	0.04	2	0.8		
29X-3, 38-39	267.58	1.35	1.32	0.03	11	3.0		
29X-4, 47-48	269.17	1.65	1.63	0.02	14			
29X-4, 59-60	269.29	0.35	0.32	0.03	3	0.7		
29X-4, 71-72	269.41	6.41	6.24	0.17	52	8.5		
29X-CC, 5-6	271.31	3.23	3.21	0.02	27	0.6		
30X-2, 10-11	275.40	3.56	3.46	0.10	29	3.3		
30X-2, 114-115	276.44	2.43	2.42	0.01	20	0.3		
30X-2, 119-120	276.49	0.18	0.17	0.01	1	0.2	1.0	
30X-4, 32-33	278.66	3.56	3.51	0.05	29	2.0		
30X-4, 39-40	278.73	0.66	0.65	0.01	5	0.2	0.1	
31X-3, 52-53	287.02	2.03	1.94	0.09	16	3.0		
31X-3, 64-65	287.14	3.66	3.45	0.21	29	7.0	1.1	
31X-4, 102-103	289.02	5.76	5.68	0.08	47	4.0	4.0	
32X-2, 46-47	295.16	0.34	0.24	0.10	2	2.5	1.6	
32X-3, 35-36	296.55	5.09	4.81	0.28	40	9.3		
32X-3, 140-141	297.60	4.92	4.51	0.41	38	8.2	1.0	
32X-4, 34-35	298.04	3.84	3.72	0.12	31	6.0	0.4	
32X-4, 40-41	298.10	5.32	5.20	0.12	43	4.0	1.3	
33X-2, 50-51	304.80	0.72	0.71	0.01	6	0.2	0.2	
33X-2, 103-104	305.33	5.96	6.14		51			
33X-4, 49-50	307.79	3.49	3.03	0.46	25	9.2	2.1	
35X-1, 86-97	323.06	8.58	8.45	0.13	70	13.0		
35X-1, 104-105	323.24	2.87	2.44	0.43	20	14.0	21.0	
35X-3, 61-62	325.81	2.53	2.12	0.41	18	8.2	1.9	
36X-1, 52-53	332.42	0.95	0.80	0.15	7	3.7	1.2	
36X-2, 16-17	333.56	8.26	7.74	0.52	65	52.0		
36X-2, 62-63	334.02	0.90	0.85	0.05	7	1.0		

Note: Concentrations of calcium carbonate were estimated from the inorganic carbon values, assuming all of the inorganic carbon was present as CaCO₃. Concentrations of organic carbon were estimated from the difference between total and inorganic carbon values. Atomic C/N and C/S ratios were calculated from organic carbon (C), total nitrogen (N), and total sulfur (S) concentrations, respectively.

depositional conditions. The unit is dominated by sediments that were displaced from shallower locations (see "Lithostratigraphy" section, this chapter), and downslope transport and rapid burial participated in delivering and preserving the organic matter.

Characterizations of Organic Matter Source

The source of organic matter in Site 898 samples was determined by either organic C/N ratios or by Rock-Eval pyrolysis. Algal organic matter generally has C/N ratios of between 5 and 10, whereas organic matter derived from land plants has values of between 20 and 100 (e.g., Emerson and Hedges, 1988; Meyers, in press). C/N ratios for samples from lithologic Unit I average 8.2 (Table 6; Fig. 20), which suggests a predominantly marine source for the organic matter in these sediments. Some Unit I samples, however, have values above 15, that reflect the probable admixture of terrigenous organic matter. The C/N values of most samples from Unit II have low ratios (<5). These values probably are an artifact of the low carbon contents, combined with the tendency of clay minerals to absorb ammonium ions generated during the degradation of organic matter (Muller, 1977). Thus, the C/N ratios in most of Unit II are not accurate indicators of organic matter source.

Rock-Eval pyrolysis of selected samples from Unit I provided further information about their organic carbon sources. Two Rock-Eval parameters are especially useful for characterizing sedimentary organic matter. The hydrogen index (HI) is the quantity of hydrocarbons generated from thermal decomposition of the organic matter, expressed as milligrams of hydrocarbons per gram of total organic carbon. Marine organic matter typically has high HI values (Espitalié et al., 1977). The oxygen index (OI) is the quantity of CO₂ generated during pyrolysis and is given in the same units. Cellulose-containing land plants produce organic matter having high OI and low HI values (Espitalié et al., 1977). Organic matter in Unit I samples has high OI and low HI values (Table 7), which normally would indicate a land-derived origin. The relatively low C/N ratios, however, contradict this

interpretation. It is likely that the organic matter has experienced considerable post-depositional oxidation, which would depress HI values while enhancing OI values. This evidence of alteration of the Rock-Eval source character implies that considerable microbial degradation of the marine organic matter in Unit I has occurred, which is consistent with an inferred history of downslope relocation of the Unit I sediments from a shallower site of initial accumulation. The generally low T_{max} values (Table 7) suggest that thermal degradation of the organic matter can be excluded; the large range (301°-441°C) observed in this parameter probably reflects heterogeneous mixtures of relatively fresh marine organic matter and detrital organic matter in the turbidites.

Headspace Gases

Concentrations of headspace methane measured in Hole 898A are displayed in Figure 21. Concentrations of methane were high in Unit I, reaching values of nearly 50,000 ppm, before decreasing to near-background levels in Unit II (Table 8). This pattern is similar to the concentrations of headspace methane measured in sediments from Site 897 (see "Site 897" chapter, this volume). Two sources of the gas in Unit I are possible. First, gas from some deeper origin may have migrated into the unit, which consists of turbiditic sand, silt, and clay layers. The location of Site 898 on a basement high makes this an especially reasonable possibility. Evidence of diffusional migration of methane into porous sediments from deeper sources was found at Sites 762 and 763 on the Exmouth Plateau passive margin of northwestern Australia (Snowdon and Meyers, 1992). In the case of Sites 762 and 763, however, a known gas source existed in underlying Jurassic rocks; a suitable deeper source for the methane at Site 898 is presently unknown. Migration of methane into the Unit I turbidite sequence, consequently, is not a strong possibility.

A second, more likely possibility is in-situ formation by methanogenic bacteria. The high values occurred in the upper Pliocene sedi-

Table 7. Results of Rock-Eval pyrolysis of selected samples from the lithologic Unit I Pliocene-Pleistocene turbidite sequence at Site 898.

Core, section, interval (cm)	Depth (mbsf)	TOC	C/N	S ₁	S ₂	S ₃	T _{max}	HI	OI
149-898B-1H-1, 22-24	0.22	0.27	9.0	0.09	0.05	2.26	307	18	837
149-898A-1H-5, 43-44	6.43	0.45	22.0	0.07	0.00	2.17		0	482
2H-4, 58-59	14.28	0.73	12.0	0.04	0.00	1.77		0	242
3H-4, 9-10	23.31	0.37	9.2	0.03	0.00	1.69		0	456
4H-2, 78-79	30.38	0.44	8.8	0.08	0.02	2.70	441	4	613
5H-5, 86-87	44.59	0.31	6.2	0.08	0.10	1.33	301	32	429
6H-6, 63-64	55.35	0.52	7.4	0.20	0.47	2.16	393	90	415
7H-6, 79-80	64.99	0.43	21.0	0.02	0.05	0.40		11	93
8H-5, 106-107	73.32	0.33	3.6	0.09	0.08	1.28		24	387
9H-4, 24-25	80.55	1.77	22.1	0.20	0.76	1.50	403	42	84
10H-3, 85-86	89.05	0.42	6.0	0.11	0.09	2.18	369	21	519
11H-1, 106-107	95.76	0.53	7.6	0.10	0.20	1.12	362	37	211
12H-3, 105-106	108.27	0.49	6.1	0.15	0.34	1.84	399	69	375
13H-3, 79-80	117.49	0.70	8.7	0.16	0.36	2.33	394	51	332
14H-5, 74-75	130.00	0.30	2.5	0.11	0.03	2.04	375	10	680
15X-2, 43-44	134.63	0.53	13.0	0.07	0.21	0.64	397	39	120
16X-1, 32-33	139.12	0.32	2.9	0.08	0.14	1.72	436	43	537
17X-2, 100-101	151.00	0.76	8.4	0.29	0.89	2.17	400	117	285

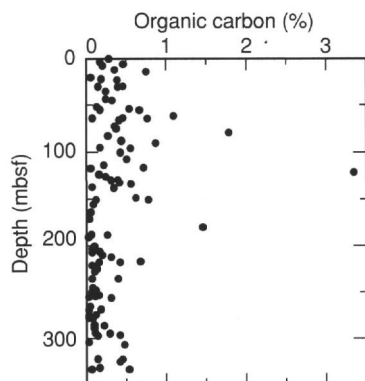


Figure 19. Concentrations of organic carbon in sediments from Holes 898A and 898B.

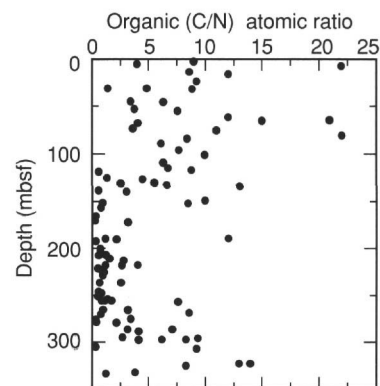


Figure 20. Organic C/N atomic ratios in sediments from Holes 898A and 898B.

ments having elevated concentrations of marine organic matter (Table 6; Fig. 19), which is prone to microbial utilization. The absence of measurable amounts of C₂ and heavier gases indicates that the gas is biogenic, as opposed to thermogenic. The source of the methane probably comes from in-situ microbial fermentation of the marine organic matter present in this turbiditic unit. Similar in-situ microbial production of methane from marine organic matter has been inferred from high biogenic gas concentrations in Pliocene-Pleistocene sediments from Site 532 on the Walvis Ridge (Meyers and Brassell, 1985) and in middle Miocene sediments from Site 767 in the Celebes Sea (Shipboard Scientific Party, 1990). The generally low amounts of organic matter and its inferred inert character in Unit II evidently preclude methanogenesis. Furthermore, Claypool and Kvenvolden (1983) observed that the presence of pore-water sulfate inhibits methanogenesis in marine sediments. High concentrations of headspace methane were not found in Site 898 sediments where pore-water sulfate concentrations were high within the upper part of Unit I and in Unit II (see "Inorganic Geochemistry" section, this chapter). This inverse relationship strengthens the possibility of the presence of active methanogenic bacterial populations in sediments as old as early Pliocene at this location.

INORGANIC GEOCHEMISTRY

Eighteen interstitial-water samples were collected at Site 898 from 3 to 336 mbsf. Samples were collected at 10-m intervals in the top 50 m

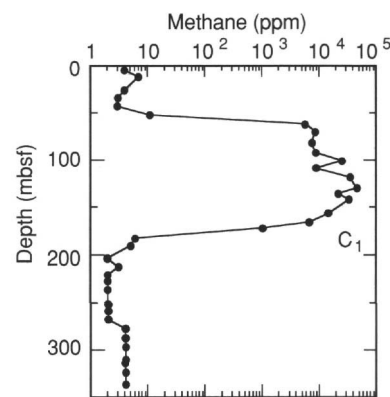


Figure 21. Profile of concentration of headspace methane in samples from Site 898.

in Hole 898A, with two additional samples collected in the top 5 m from Hole 898B. Samples were collected at 30-m intervals between 50 and 336 mbsf. A slightly higher sampling density was used in the interval between 148 and 187 mbsf. Results from shipboard interstitial-water analyses are presented in Table 9.

Interstitial-water samples spanned lithologic Unit I through Subunit IIB. As was the case at Site 897, the most significant changes in interstitial-water chemistry occurred at the boundary between Unit I

Table 8. Results of headspace gas analyses from Hole 898A.

Core, section, interval (cm)	Depth (mbsf)	C ₁
149-898A-		
1H-5, 7-12	6.10	4
2H-4, 0-5	13.73	7
3H-6, 0-5	26.23	4
4H-6, 0-5	35.73	3
5H-5, 0-5	43.73	3
6H-5, 0-5	53.23	11
7H-5, 0-5	62.73	6,308
8H-4, 0-5	70.73	9,454
9H-5, 0-5	81.73	8,149
10H-5, 0-5	91.23	9,737
11H-5, 0-5	100.73	27,073
12H-4, 0-5	108.73	9,640
13H-4, 0-5	118.23	38,490
14H-5, 0-5	129.23	49,484
15X-3, 0-5	135.73	24,336
16X-3, 0-5	141.83	35,629
17X-6, 0-5	156.03	15,944
18X-6, 0-5	165.63	7,130
19X-4, 0-5	172.33	1,085
20X-4, 0-5	181.93	6
21X-3, 0-5	190.03	5
22X-6, 0-5	204.23	2
23X-5, 0-5	212.43	3
24X-4, 0-5	220.93	2
25X-2, 0-5	227.13	2
26X-2, 0-5	236.73	2
27X-5, 0-5	250.83	2
28X-4, 0-5	259.03	2
29X-3, 0-5	267.23	2
30X-3, 0-5	276.83	4
31X-3, 0-5	286.53	4
32X-3, 0-5	296.23	4
33X-6, 0-5	309.93	4
34X-1, 145-150	313.98	4
35X-2, 0-5	323.73	4
36X-4, 0-5	336.43	4

Note: Methane (C₁) concentrations are given in parts per million. Heavier gases were not measureable in Hole 898A headspace samples.

and Subunit IIA. However, this boundary occurred shallower in the sediment column at Site 898 than at Site 897.

Pleistocene and Pliocene sediments are dominated by turbidite sequences relatively rich in organic carbon. In contrast, Miocene through Eocene sediments are depleted of reactive carbon (see "Organic Geochemistry" section, this chapter).

Concentrations of sulfate decrease linearly from 26 mM in the first sample, at 3 mbsf, to near 0 mM by 71 mbsf (Fig. 22A). The gradient in concentration indicates downward diffusion of bottom-water sulfate to a zone of sulfate reduction (removal) between 71 and 152 mbsf. Sulfate concentrations remain near zero through Unit I (which extends down to 163 mbsf; see "Lithostratigraphy" section, this chapter), but increase below the boundary between Unit I and Subunit IIA (around 170 mbsf). The increase in sulfate concentrations below 170 mbsf indicate diffusion of sulfate from a deep reservoir to the base of the Pleistocene and Pliocene sequences. As was the case at Site 897, the deep sulfate reservoir has been preserved by the relatively slow sediment accumulation rates during the Miocene (see "Lithostratigraphy" section, this chapter). Below the sulfate minimum sulfate concentrations reach their maximum values (15-16 mM) between 296 mbsf and the deepest core sample at 336 mbsf.

Alkalinity increases linearly from about 4 mM at 3 mbsf to 16 mM at 40 mbsf (Fig. 22B). Alkalinity remains nearly constant between 44 and 101 mbsf and increases to a broad maximum between 129 and 156 mbsf. The increase in alkalinity above 156 mbsf results from organic carbon degradation through sulfate reduction (Gieskes, 1974, 1983). Below the zone of sulfate reduction, alkalinity generally decreases; however, alternating zones of removal and release are indicated by a small dip in concentration at 190 mbsf, followed by a peak at 237 mbsf.

Concentrations of ammonia increase linearly from a concentration of 447 μ M at 3 mbsf to a broad maximum of greater than 3000 μ M

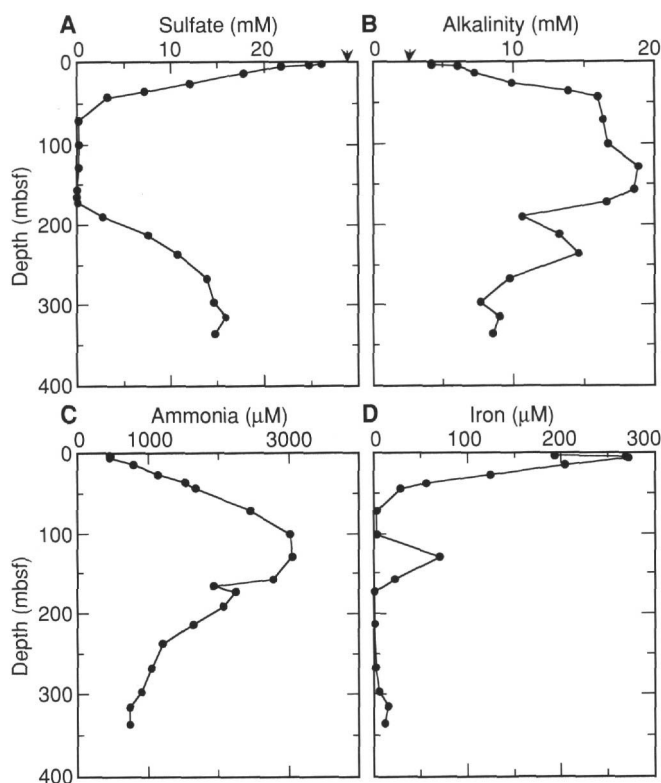


Figure 22. Interstitial-water profiles for Site 898. Arrows indicate typical bottom-water values. A. Sulfate. B. Alkalinity. C. Ammonia. D. Iron.

between 101 and 129 mbsf (Fig. 22C). The production of ammonia in sediments results from anoxic carbon degradation; thus, the changes in the ammonia profile at this site are inverse to changes in the sulfate profile. The highest concentrations of ammonia can be observed in the Pleistocene and Pliocene sediments of Unit I, coincident with the sulfate minimum. Ammonia concentrations decrease below 129 mbsf to concentrations less than 800 μ M at the deepest section cored (336 mbsf).

Concentrations of dissolved iron increase from 193 μ M at 3 mbsf to a maximum of 272 μ M by 6 mbsf (Fig. 22D). Below the maximum, iron concentrations decrease linearly to near zero between 71 and 101 mbsf, coincident with the shallowest zone of sulfate reduction. The maximum can be attributed to the release of iron caused by reduction to the soluble Fe⁺² state during the decomposition of organic carbon. Iron concentrations increase below 100 mbsf to 70 μ M, but return to zero by 172 mbsf and remain low throughout the remainder of the cored sediments.

Concentrations of dissolved manganese increase from ~90 μ M at 3 mbsf to a maximum of ~130 μ M by 4 mbsf (Fig. 23A). Below the maximum, concentrations of manganese decrease to near 0 μ M between 36 and 190 mbsf. The maximum can be attributed to the release of manganese as a result of reduction to the soluble Mn⁺² state during the decomposition of organic carbon. Manganese concentrations remain near zero through the remainder of Unit I (~160 mbsf), but increase below 190 mbsf. The anomalously high concentrations at 172 mbsf are probably the result of sample contamination. Concentrations of manganese increase below 190 mbsf, resulting in a small peak of between 237 and 267 mbsf, followed by a zone of removal at about 300 mbsf.

In Unit I, concentrations of calcium show depletion (30%-60%), with respect to present bottom-water concentrations, down to about 160 mbsf (Fig. 23B). The depletion in calcium is coincident with the

Table 9. Interstitial-water data for Site 898.

Core, section, interval (cm)	Depth (mbsf)	Alkalinity (mM)	Sulfate (mM)	Chloride (mM)	Iron (μM)	Sodium (mM)	Potassium (mM)	Magnesium (mM)	Calcium (mM)	Ammonia (μM)	Silica (μM)	Manganese (μM)	Strontium (μM)
149-898A-													
1H-5, 0-7	6.0	5.99	21.8	567	272	490	12.2	53.0	9.6	443	224	34.3	82
2H-3, 143-150	13.7	7.24	17.8	514	204	443	11.5	47.9	7.0	789	293	6.0	84
3H-5, 143-150	26.2	9.88	12.1	531	125	497	11.3	46.1	5.8	1143	337	1.5	85
4H-5, 143-150	35.7	13.87	7.2	518	55	492	10.8	43.7	5.2	1524	376	0	84
5H-4, 143-150	43.7	15.97	3.2	519	28	479	8.9	42.7	4.7	1677	402	0	90
8H-3, 143-150	70.7	16.36	0.2	523	3	476	9.6	40.0	5.5	2451	672	0	102
11H-4, 143-150	100.7	16.73	0.2	531	2	492	10.3	39.8	6.4	3021	432	0	119
14H-4, 143-150	129.2	18.88	0.2	512	70	484	10.1	40.0	7.2	3053	695	0	144
17X-5, 143-150	156.0	18.52	0.0	543	22	487	9.7	41.5	8.7	2782	1073	0.5	185
18X-5, 143-150	165.6		0.0	574		473	6.9	45.3	9.9	1921	916		221
19X-3, 135-150	172.2	16.59	0.1	558	0	478	8.4	43.4	9.8	2251	789	85.0	218
21X-2, 135-150	189.9	10.57	2.8	572		482	9.4	42.2	12.6	2078	1039	0.5	250
23X-4, 135-150	212.3	13.24	7.6	580	0	480	8.9	44.0	15.1	1642	1105	11.0	253
26X-1, 135-150	236.6	14.64	10.7	574		479	8.2	44.5	19.6	1210	1129	21.5	261
29X-2, 135-150	267.1	9.75	13.8	561	1	475	7.9	43.7	22.9	1044	1071	19.5	303
32X-2, 135-150	296.1	7.63	14.6	615	5	494	8.5	43.7	26.9	899	1011	5.0	353
34X-2, 0-16	314.1	9.01	15.9	567	15	474	6.1	42.6	27.9	738	1147	2.5	399
36X-3, 135-150	336.3	8.52	14.7	571	11	484	6.6	40.9	27.8	746	1009	10.0	399
149-898B-													
1H-3, 0-15	3.08	4.16	26.1	565	193	490	12.5	54.9	10.8	447	201	87.5	86
1H-3, 140-150	4.45	4.16	24.8	558	268	489	11.4	55.3	10.1	467	175	135.5	85

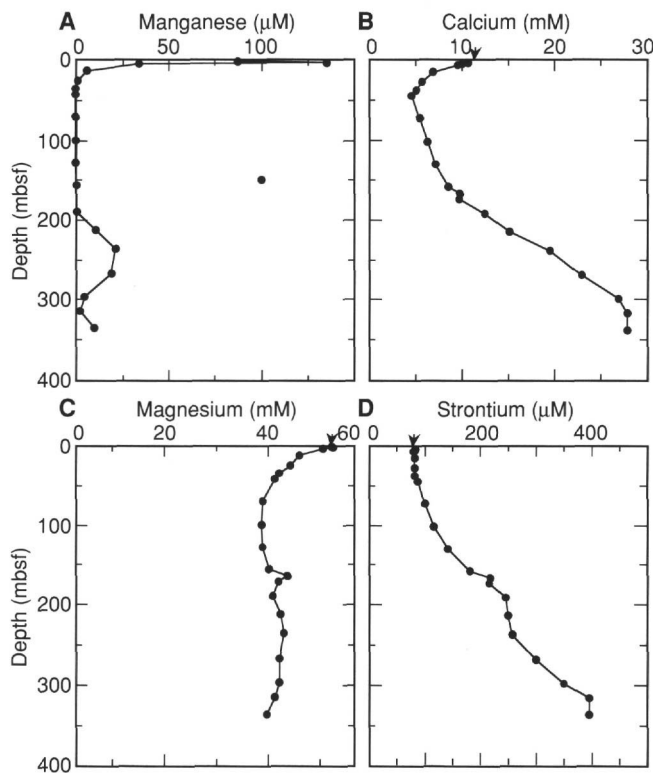


Figure 23. Interstitial-water profiles for Site 898. Arrows indicate typical bottom-water values. A. Manganese. B. Calcium. C. Magnesium. D. Strontium.

zone of maximum alkalinity and probably reflects precipitation of a carbonate phase. Concentrations of calcium increase below 160 mbsf to constant values of about 30 μM below 296 mbsf. The release of calcium between 160 and 336 mbsf probably reflects a region of silicate mineral alteration and/or carbonate dissolution.

Concentrations of magnesium show some depletion with respect to bottom water throughout the sediment column, with the greatest depletion (~30%) coinciding with the zone of calcium depletion (Fig. 23C). Concentrations of magnesium increase slightly below 160 mbsf.

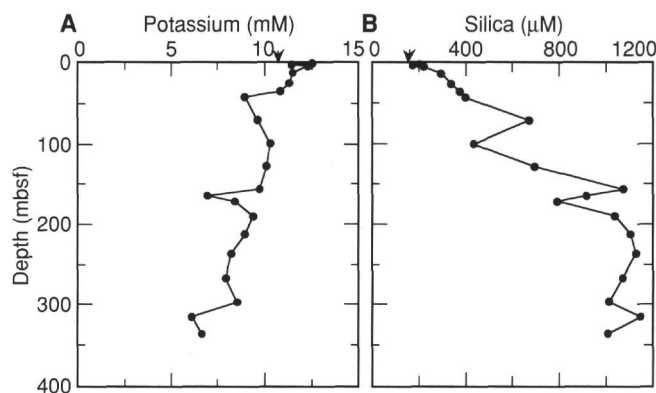


Figure 24. Interstitial-water profiles for Site 898. Arrows indicate typical bottom-water values. A. Potassium. B. Silica.

Concentrations of strontium generally increase with depth from a minimum of about 80 μM near the sediment surface to a maximum of ~400 μM at 314 and 336 mbsf (Fig. 23D). The strontium profile is concave up between the surface and 172 mbsf, indicating removal, with some release occurring in Unit II, between 172 and 190 mbsf. The strontium profile also is concave up between 190 and 314 mbsf, again indicating removal. The concentration maximum at the base of the profile indicates a second zone of the release of strontium to the interstitial waters. Release of strontium is probably associated with recrystallization of carbonate phases (Gieskes, 1974).

In general, concentrations of potassium decrease through the sediment column, with some narrow zones of release and removal indicated by fluctuations in the gradient (Fig. 24A). Values of potassium decrease from a maximum of 12.5 mM near the seafloor to a minimum of about 6 mM below 300 mbsf. The slight enrichment in potassium (with respect to bottom water) near the seafloor may be the result of temperature-of-squeezing effects (Sayles et al., 1973). Possible artifacts in concentrations of potassium resulting from this effect could not be verified because of failure of the in-situ sampler.

Concentrations of silica generally increase with depth, but indicate alternating zones of release and removal that produced small peaks at about 70 and 160 mbsf and a broad high below 190 mbsf (Fig. 24B). Concentrations of silica are elevated (up to 700 μM) with respect to bottom water through much of the Pleistocene sequences. Silica has been removed from the interstitial water at about 100 mbsf and again

near the boundary between Unit I and Subunit IIA (~172 mbsf). Silica concentrations show release through the Miocene sequence, which resulted in a broad maximum approaching 1100 μM through the remainder of the cored sequence.

Concentrations of chloride show slight depletion with respect to seawater through Unit I (extending down to 163 mbsf) and return to near bottom-water values below (Table 9). In contrast to concentrations of chloride, concentrations of sodium show little variation with depth, with the exception of a single interval at 20 mbsf that is slightly depleted with respect of bottom water (Table 9).

PHYSICAL PROPERTIES

Introduction

Measurements of whole cores taken at Site 898 included magnetic susceptibility, Gamma-Ray Attenuation Porosity Evaluator (GRAPE) bulk densities, *P*-wave-logger (PWL) velocities, and thermal conductivity. Reliable velocities were obtained in un lithified sediments using the Digital Sound Velocimeter (DSV) on split cores and, within the more consolidated units, using the Hamilton Frame Velocimeter. Electrical resistivity and undrained shear strength were measured on split cores. Index properties were calculated from wet and dry masses and wet and dry volumes. Physical-properties data generally show uniform downhole trends for the 342 m of Hole 898 A. Only one APC-core was taken at Hole 898B. Data from this core are discussed together with the data from Hole 898A.

Index Properties

Index properties were determined using gravimetric methods (Table 10; Fig. 25). Densities also were determined, with an uncertainty of $\pm 0.02 \text{ g/cm}^3$. The accuracy of the porosity measurements has been estimated as 2%. Bulk and grain densities and porosity distributions indicate smooth downhole trends. Gravimetrically determined bulk densities increase from about 1.7 g/cm^3 near the seafloor to 2.0 g/cm^3 at a depth of 339 mbsf. Porosities decrease from about 65% at the seafloor to 49% at the base of the hole. Grain densities are nearly constant with depth and have a mean value of 2.78 g/cm^3 .

The excellent APC-core recovery in the upper 132 m of Hole 898 A preserved thick sand units, which provided us an opportunity to sample systematically both clay- and sand-rich lithologies and to compare their respective index properties. However, sand units near the top of the sediment section were soupy and had been disturbed by

drilling; therefore, the calculated porosities must be viewed with caution. Porosities obtained from discrete sand samples are indicated in Figure 25 as open diamonds. Porosities in sands generally are lower than those for clay-rich units (Hamilton, 1976), and range from about 50% to 55% in the upper 150 m of the hole.

GRAPE Measurements

Bulk densities were estimated also from whole-core GRAPE measurements taken on all sections recovered from Holes 898A and 898B (see "Explanatory Notes" chapter, this volume). The maximum GRAPE densities give the best estimate for true bulk density of the sediment (Boyce, 1973; Gealy, 1971). The visually estimated maximum densities are indicated by the line superimposed on the Gravimetric Bulk Density and GRAPE Bulk Density graphs in Figure 25. The line shows a slight net decrease in bulk density with depth. This contrasts with the gravimetrically determined bulk density, which shows an increase down the hole from 1.7 g/cm^3 near the seafloor to 2.0 g/cm^3 at 339 mbsf (Fig. 25). The GRAPE density appears to be high relative to the average gravimetric density near the top of the hole and low near the base of the hole. This discrepancy is probably related, in part, to incompletely filled liners in the deeper XCB cores.

Electrical Resistivity

Electrical resistivity was measured at intervals of 0.5 to 0.75 m in all split cores down to 340 mbsf. Formation factors calculated from the resistivity data (see "Explanatory Notes" chapter, this volume) show a general increase with depth (Fig. 25). In the upper 230 m of sediment, the formation factor ranges from 4 to 6, defining a fairly linear downhole trend. Below 230 mbsf, the formation factor is consistently higher and exhibits a large scatter between 5 and 15. This scatter can be attributed to the presence of less porous nanofossil clays (see "Lithostratigraphy" section, this chapter).

Undrained Shear Strength

Using the vane shear apparatus, undrained shear strength was measured in cores from the upper 260 m of Hole 898A at a frequency of one measurement per core (Fig. 26). Shear strengths ranged from about 6 kPa at a depth of 2 mbsf (Core 149-898A-1H) to a maximum of 122 kPa at 162 mbsf (Core 149-898A-18X). The scatter of the

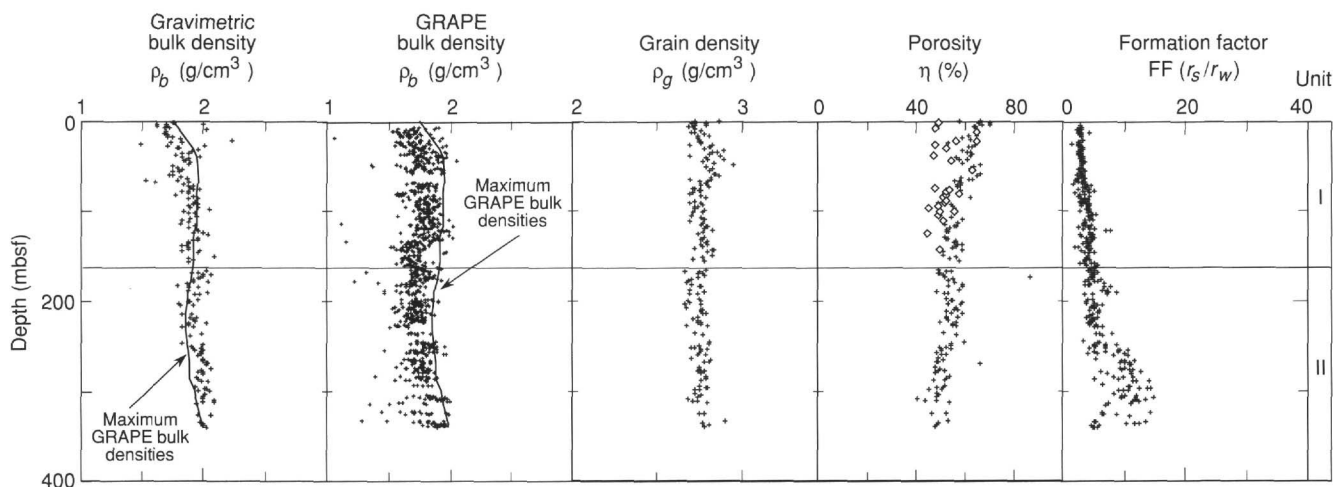


Figure 25. Gravimetrically determined bulk density, GRAPE-estimated bulk density, gravimetrically determined grain density, porosity, and formation factor data for core samples from Holes 898A and 898B. Open diamonds indicate the porosity of sands. The horizontal line is the boundary between lithostratigraphic Units I and II. The lines on the bulk density graphs are the visually estimated maximum GRAPE bulk density.

Table 10. Index properties data from Hole 898A and 898B.

Core, section, interval (cm)	Depth (mbsf)	Sample wet mass (g)	Sample wet vol. (cm ³)	Sample dry mass (g)	Sample dry vol. (cm ³)	Bulk density (g/cm ³)	Grain density (g/cm ³)	Porosity (%)	Water content (% dry mass)
149-898A-									
1H-1, 79-81	0.79	13.47	7.64	7.03	2.57	1.76	2.75	57.29	98.15
1H-2, 51-53	2.01	11.43	6.78	6.87	2.53	1.69	2.73	61.20	70.53
1H-3, 79-81	3.79	10.00	6.19	5.54	2.03	1.62	2.75	65.74	85.98
1H-4, 92-94	5.42	12.37	7.19	7.68	2.81	1.72	2.74	59.56	64.72
1H-5, 85-87	6.85	13.18	7.83	8.10	3.00	1.68	2.71	60.98	66.53
1H-6, 145-147	8.95	9.59	4.74	7.28	2.65	2.02	2.75	42.25	33.28
2H-1, 54-56	9.74	14.27	8.43	8.81	3.18	1.69	2.78	62.03	65.71
2H-2, 64-66	11.34	11.87	7.01	7.28	2.68	1.69	2.73	60.82	66.87
2H-3, 65-67	12.85	13.40	7.96	8.19	2.99	1.68	2.75	61.85	67.47
2H-4, 39-41	14.09	11.96	7.00	7.40	2.66	1.71	2.80	61.42	65.35
2H-5, 25-27	15.45	13.60	8.02	8.42	2.99	1.70	2.83	62.87	65.22
2H-6, 44-46	17.14	13.00	7.42	8.40	3.05	1.75	2.76	58.22	57.92
3H-1, 35-37	19.05	13.40	7.41	8.99	3.27	1.81	2.76	54.82	51.76
3H-1, 84-86	19.54	12.76	5.73	8.15	2.96	2.23	2.77	31.03	59.82
3H-2, 105-107	21.25	8.78	5.08	5.40	1.96	1.73	2.78	59.73	66.32
3H-3, 121-123	22.91	14.01	7.70	9.70	3.51	1.82	2.77	54.53	46.78
3H-4, 83-85	24.03	11.19	7.57	8.04	2.90	1.48	2.78	74.17	41.21
3H-5, 103-105	25.73	12.57	7.35	7.86	2.78	1.71	2.85	62.34	63.50
3H-6, 88-90	27.08	10.98	5.47	8.32	3.06	2.01	2.72	42.20	33.52
3H-7, 20-22	27.90	10.54	5.89	6.85	2.43	1.79	2.83	57.66	56.98
4H-1, 95-96	29.15	6.89	3.83	4.40	1.56	1.80	2.84	57.29	59.87
4H-2, 63-64	30.33	7.45	3.81	5.42	1.94	1.95	2.80	47.60	39.32
4H-3, 60-61	31.80	5.08	2.67	3.45	1.19	1.90	2.92	53.62	49.89
4H-4, 99-100	33.69	6.96	3.81	4.47	1.58	1.83	2.85	55.94	58.94
4H-5, 88-89	35.08	5.29	2.81	3.47	1.21	1.88	2.88	53.77	55.47
4H-6, 41-42	36.11	8.03	4.54	5.12	1.82	1.77	2.83	58.79	60.20
4H-7, 32-33	37.52	5.46	2.99	3.53	1.23	1.83	2.90	57.02	57.74
5H-1, 110-112	38.80	14.71	7.45	11.18	4.11	1.97	2.72	44.17	33.11
5H-2, 53-55	39.73	9.90	5.26	6.88	2.46	1.88	2.81	51.94	46.23
5H-3, 95-97	41.65	10.33	5.60	7.10	2.53	1.85	2.82	54.31	47.93
5H-4, 112-113	43.32	6.70	3.65	4.44	1.53	1.84	2.92	57.19	53.80
5H-5, 115-117	44.85	10.82	5.73	7.66	2.76	1.89	2.79	50.95	43.40
5H-6, 116-118	46.36	7.28	3.86	4.93	1.73	1.88	2.86	53.09	50.29
6H-2, 65-66	49.35	6.45	3.68	3.98	1.35	1.75	2.98	62.61	65.74
6H-3, 81-83	51.01	6.12	3.44	3.85	1.38	1.78	2.81	57.67	62.48
6H-4, 46-47	52.16	6.15	3.36	3.98	1.40	1.83	2.85	55.98	57.63
6H-5, 94-95	54.14	7.52	4.18	4.83	1.72	1.80	2.83	56.97	58.88
6H-6, 67-68	55.37	9.67	5.54	6.18	2.20	1.75	2.83	59.98	59.71
7H-1, 115-116	57.85	8.29	4.82	5.05	1.77	1.72	2.86	62.28	68.08
7H-2, 81-82	59.01	6.36	3.63	3.85	1.35	1.75	2.87	60.57	69.14
7H-3, 105-106	60.75	6.57	3.64	4.09	1.43	1.81	2.89	57.95	64.20
7H-4, 76-77	61.96	7.18	3.87	4.87	1.72	1.86	2.84	54.33	49.97
7H-5, 93-94	63.63	5.44	3.05	3.47	1.23	1.79	2.84	58.16	60.09
7H-6, 118-119	65.38	6.58	4.32	4.21	1.55	1.52	2.72	70.68	59.52
7H-7, 41-42	66.11	5.92	3.70	4.02	1.46	1.60	2.77	66.92	49.79
8H-1, 68-70	66.88	9.95	5.31	6.98	2.49	1.88	2.82	52.57	44.77
8H-2, 58-60	68.28	8.44	4.58	5.74	2.05	1.84	2.81	54.22	49.56
8H-3, 97-98	70.17	5.76	3.01	3.88	1.40	1.91	2.78	49.39	51.07
8H-4, 73-74	71.43	9.67	5.13	6.69	2.38	1.88	2.82	52.09	46.95
8H-5, 45-46	72.68	8.73	4.63	6.01	2.13	1.89	2.83	52.41	47.71
8H-6, 110-112	74.83	12.88	6.54	9.73	3.56	1.97	2.74	44.94	33.94
8H-7, 20-21	75.43	9.95	5.18	7.08	2.59	1.92	2.75	47.85	42.64
9H-1, 64-66	76.34	8.85	4.84	5.96	2.16	1.83	2.77	53.99	51.17
9H-2, 39-41	77.59	12.00	6.38	8.57	3.09	1.88	2.78	51.30	42.08
9H-3, 54-56	79.35	11.85	6.29	8.58	3.14	1.88	2.74	49.90	40.03
9H-4, 52-54	80.83	12.97	7.34	8.75	3.23	1.77	2.72	56.15	50.86
9H-5, 35-37	82.16	11.80	6.16	8.58	3.09	1.91	2.78	49.38	39.43
9H-6, 112-114	84.43	9.51	5.09	6.12	2.19	1.87	2.81	52.73	58.57
9H-7, 52-54	85.33	10.18	5.22	7.48	2.67	1.95	2.81	48.17	37.93
10H-2, 117-119	87.87	11.56	5.99	8.33	3.04	1.93	2.75	47.52	40.78
10H-3, 128-130	89.48	9.58	4.99	6.70	2.40	1.92	2.80	49.57	45.26
10H-4, 68-70	90.38	11.99	6.23	8.67	3.20	1.92	2.72	46.81	40.22
10H-5, 54-56	91.74	14.48	7.38	10.86	3.92	1.96	2.78	46.51	34.96
10H-6, 109-111	93.79	13.01	6.94	9.22	3.32	1.88	2.79	51.80	43.25
10H-7, 25-27	94.45	13.26	6.78	9.94	3.61	1.96	2.76	46.37	35.05
11H-1, 61-63	95.31	12.96	6.86	9.12	3.33	1.89	2.75	49.85	44.29
11H-2, 90-92	97.10	15.48	7.58	12.04	4.39	2.04	2.75	40.97	29.93
11H-3, 35-37	98.05	12.62	6.86	8.75	3.13	1.84	2.80	54.23	46.59
11H-4, 115-117	100.35	14.26	7.38	10.58	3.87	1.93	2.74	47.13	36.51
11H-5, 110-111	101.80	12.18	6.49	8.52	3.06	1.88	2.79	51.86	45.23
11H-6, 21-23	102.41	13.27	7.10	9.30	3.35	1.87	2.78	52.02	44.93
12H-1, 94-96	105.14	14.52	7.49	10.86	3.99	1.94	2.73	46.37	35.36
12H-2, 106-107	106.76	11.88	6.29	8.44	3.04	1.89	2.78	50.94	42.89
12H-4, 98-100	109.68	14.56	7.94	9.77	3.51	1.83	2.80	54.32	51.72
12H-5, 75-77	110.95	15.53	8.25	11.34	4.17	1.88	2.72	49.58	38.82
12H-6, 109-111	112.79	15.34	8.48	10.54	3.80	1.81	2.79	55.45	47.97
13H-1, 77-79	114.47	11.31	5.86	8.27	2.98	1.93	2.78	48.52	38.59
13H-2, 94-95	116.14	9.55	5.09	6.64	2.37	1.88	2.81	52.38	46.13
13H-3, 66-68	117.36	8.45	4.49	5.91	2.10	1.88	2.82	52.36	45.22
13H-4, 114-115	119.34	7.28	3.75	5.22	1.87	1.94	2.80	48.34	41.48
13H-5, 84-86	120.54	9.16	4.70	6.66	2.35	1.95	2.85	49.23	39.44
13H-6, 102-103	122.22	7.45	3.74	5.37	1.93	1.99	2.79	45.19	40.70
14H-1, 77-79	123.97	11.20	5.86	8.11	2.91	1.91	2.79	49.92	40.03
14H-2, 121-122	125.91	11.91	5.86	9.32	3.38	2.03	2.76	44.18	29.11
14H-3, 92-94	127.12	9.56	5.31	6.44	2.32	1.80	2.79	56.00	51.10
14H-4, 54-56	128.24	11.72	6.01	8.57	3.07	1.95	2.80	47.91	38.60

Table 10 (continued).

Core, section, interval (cm)	Depth (mbsf)	Sample wet mass (g)	Sample wet vol. (cm ³)	Sample dry mass (g)	Sample dry vol. (cm ³)	Bulk density (g/cm ³)	Grain density (g/cm ³)	Porosity (%)	Water content (% dry mass)
14H-5, 102-104	130.22	9.01	4.62	6.50	2.35	1.95	2.78	47.15	40.61
14H-6, 95-97	131.65	11.70	6.11	8.43	3.04	1.92	2.79	49.38	40.75
15X-1, 65-67	133.35	11.32	6.02	7.86	2.80	1.88	2.82	52.27	46.35
15X-2, 60-62	134.80	10.19	5.45	7.14	2.55	1.87	2.81	52.64	44.94
15X-3, 119-121	136.89	9.69	5.21	6.64	2.40	1.86	2.78	52.38	48.43
15X-4, 44-46	137.64	11.30	6.20	7.61	2.71	1.82	2.82	55.55	51.14
16X-1, 110-112	139.90	9.67	5.17	6.69	2.40	1.87	2.79	52.27	46.92
16X-2, 113-115	141.43	12.01	6.38	8.44	3.08	1.88	2.75	50.27	44.52
16X-3, 67-68	142.47	13.47	6.85	10.07	3.54	1.97	2.85	48.50	35.43
16X-4, 77-79	144.07	9.43	5.17	6.37	2.24	1.83	2.86	56.40	50.64
16X-5, 61-62	145.41	10.76	5.50	7.93	2.83	1.96	2.82	47.87	37.45
17X-1, 130-131	149.80	6.62	3.19	4.91	1.73	2.08	2.85	42.41	36.55
17X-2, 76-78	150.76								
17X-3, 55-57	152.05	10.23	5.44	7.06	2.54	1.88	2.79	51.51	47.27
17X-4, 29-31	153.29	9.95	5.18	7.07	2.59	1.92	2.74	47.75	42.85
17X-5, 37-38	154.87	8.01	4.27	5.47	1.96	1.88	2.80	52.13	48.98
17X-6, 134-136	157.34								
18X-1, 101-103	159.11		4.92	6.58	2.36		2.74		
18X-2, 109-111	160.69		7.22	10.44	3.73		2.76		
18X-3, 118-120	162.28		5.29	8.24	2.64		3.05		
18X-4, 107-109	163.67		5.38	7.28	2.63		2.73		
18X-5, 107-109	165.17	10.52	5.19	7.88	2.81	2.02	2.81	43.90	35.16
18X-6, 120-121	166.80	12.34	6.33	8.88	3.31	1.95	2.69	44.50	40.98
18X-7, 28-30	167.38	10.33	5.42	7.30	2.64	1.90	2.77	49.63	43.69
19X-1, 102-104	168.82	11.35	5.67	8.40	3.06	2.00	2.76	43.48	36.85
19X-2, 85-87	170.15	13.02	6.31	9.79	3.52	2.06	2.79	41.15	34.61
19X-3, 88-89	171.68	8.62	4.31	6.32	2.27	2.00	2.80	44.85	38.19
19X-4, 112-113	173.42	11.18	5.72	8.11	2.95	1.95	2.76	46.32	39.78
19X-5, 75-76	174.55	12.16	6.16		3.25	1.97			
19X-6, 72-73	176.02	9.24	4.84	6.46	2.38	1.91	2.73	47.98	45.31
19X-7, 27-28	177.07	9.06	4.47		2.39	2.03			
20X-1, 112-113	178.52	9.69	5.06	6.94	2.56	1.91	2.71	47.40	41.66
20X-2, 91-92	179.81	10.91	5.86	7.57	2.82	1.86	2.70	49.86	46.47
20X-3, 110-111	181.50	9.48	5.33	6.29	2.32	1.78	2.73	55.62	53.51
20X-4, 89-90	182.79	10.47	5.36	7.54	2.74	1.96	2.77	46.54	40.83
20X-5, 43-44	183.83	10.57	5.66	7.10	2.56	1.87	2.78	52.11	51.57
21X-1, 111-112	188.11	8.76	4.69	5.94	2.19	1.87	2.72	50.30	50.04
21X-2, 107-109	189.57	11.01	5.44	8.30	2.98	2.03	2.80	43.53	34.25
21X-3, 140-141	191.40	8.81	4.47	6.39	2.35	1.97	2.72	44.37	39.78
21X-4, 39-14	191.89	10.97	5.69	7.85	2.85	1.93	2.76	48.04	41.77
22X-1, 127-129	197.97	9.60	4.90	6.97	2.52	1.96	2.77	46.60	39.59
22X-2, 109-111	199.29	10.08	5.34	7.10	2.56	1.89	2.78	50.91	44.16
22X-3, 68-69	200.38	10.62	5.67	7.46	2.76	1.87	2.71	49.72	44.59
22X-4, 53-56	201.73	12.64	7.03	8.40	3.10	1.80	2.72	54.33	53.29
22X-5, 36-38	203.06	9.95	5.49	6.64	2.48	1.81	2.69	52.65	52.64
22X-6, 55-57	204.75	12.10	6.31	8.70	3.14	1.92	2.78	49.15	41.07
23X-1, 110-112	207.50	12.68		8.68	3.23		2.70		48.55
23X-2, 113-115	209.03	9.28		6.37	2.30		2.78		48.11
23X-3, 94-95	210.34	10.09		7.06	2.53		2.79		45.19
23X-4, 85-87	211.75	12.32		8.91	3.21		2.78		40.24
23X-5, 121-123	213.61	10.95	5.97	7.37	2.65	1.83	2.79	54.16	51.25
23X-6, 70-72	214.60	12.31	6.49	8.76	3.13	1.90	2.81	51.15	42.62
24X-1, 60-61	217.00	8.38	4.44	5.76	2.09	1.89	2.76	50.41	47.90
24X-2, 81-83	218.71	9.92	5.12	7.17	2.61	1.94	2.76	47.26	40.28
24X-3, 42-44	219.82	10.26	5.37	7.41	2.71	1.91	2.74	48.41	40.45
24X-4, 79-81	221.69	11.77	6.11	8.47	3.08	1.93	2.76	47.98	40.95
24X-5, 77-78	223.17	6.85	3.39	5.10	1.85	2.02	2.76	42.68	35.98
24X-6, 28-30	224.18	9.53	5.09	6.57	2.37	1.87	2.78	51.74	47.44
25X-1, 38-40	225.98	10.29	5.48	7.25	2.61	1.88	2.78	51.57	44.11
25X-2, 93-96	228.05	9.95	5.42	6.83	2.53	1.83	2.70	51.79	48.16
25X-3, 23-25	228.86	7.33	3.84	5.18	1.85	1.91	2.82	50.53	43.66
26X-1, 55-57	235.75	7.60	3.85	5.58	2.04	1.98	2.75	44.81	38.01
26X-2, 53-54	237.23	7.44	3.93	5.15	1.85	1.89	2.79	50.89	46.87
27X-1, 40-41	245.20	7.64	4.18	5.08	1.80	1.83	2.83	55.58	53.17
27X-2, 77-78	247.07	7.97	4.25	5.45	1.96	1.88	2.80	51.91	48.76
27X-3, 130-131	249.10	6.63	3.33	4.71	1.67	1.99	2.83	46.55	42.92
27X-4, 78-81	250.08	11.74	6.17	8.30	3.01	1.90	2.77	49.59	43.63
27X-5, 56-57	251.36	10.47	5.28	7.78	2.86	1.98	2.73	43.69	36.28
27X-6, 53-54	252.83	12.05	6.28	8.68	3.17	1.92	2.75	48.10	40.83
27X-7, 22-23	254.02	10.51	5.27	7.78	2.77	1.99	2.82	45.88	36.82
28X-1, 46-47	254.96	8.44	4.37	5.98	2.16	1.93	2.78	48.31	43.26
28X-2, 115-117	257.15	12.08	6.10	8.95	3.23	1.98	2.78	45.50	36.69
28X-3, 105-106	258.55	13.20	6.67	9.93	3.60	1.98	2.77	45.21	34.55
28X-4, 99-100	259.99	12.13	6.19	8.95	3.25	1.96	2.76	46.14	37.30
28X-5, 36-37	260.86	11.17	5.72	8.09	2.89	1.95	2.81	48.01	40.02
29X-1, 95-96	265.15	9.36	4.68	6.99	2.57	2.00	2.73	42.73	35.56
29X-2, 85-86	266.55	11.70	5.86	8.64	3.06	2.00	2.84	46.27	37.18
29X-3, 111-112	268.31	9.80	4.83	7.38	2.65	2.03	2.80	43.23	34.38
29X-4, 69-70	269.39	9.95	4.92	7.53	2.67	2.02	2.83	44.73	33.70
29X-5, 97-98	271.17	10.56	5.24		2.80	2.02			
30X-1, 146-147	275.26	11.69	5.68	8.85	3.20	2.06	2.77	40.86	33.64
30X-2, 84-85	276.14	12.58	6.35	9.33	3.38	1.98	2.77	45.13	36.56
30X-3, 98-99	277.78	12.10	6.08	9.08	3.25	1.99	2.80	45.65	34.89
30X-4, 88-89	279.18	11.67	5.96	8.50	3.09	1.96	2.76	46.20	39.20
30X-5, 42-43	280.22	14.33	7.16	10.84	3.91	2.00	2.78	44.32	33.77
31X-1, 96-97	284.46	10.92	5.64	7.81	2.79	1.94	2.81	48.91	41.90
31X-2, 80-81	285.80	11.96	6.14	8.66	3.09	1.95	2.81	48.33	40.05

Table 10 (continued).

Core, section, interval (cm)	Depth (mbsf)	Sample wet mass (g)	Sample wet vol. (cm ³)	Sample dry mass (g)	Sample dry vol. (cm ³)	Bulk density (g/cm ³)	Grain density (g/cm ³)	Porosity (%)	Water content (% dry mass)
31X-3, 134-135	287.84	11.41	5.78	8.33	3.01	1.98	2.78	45.82	38.82
31X-4, 94-95	288.94	12.98	6.38	9.94	3.58	2.03	2.78	42.57	32.06
32X-1, 119-120	294.39	9.24	4.78	6.74	2.44	1.93	2.77	47.96	38.94
32X-2, 107-108	295.77	10.94	5.41	8.27	2.95	2.02	2.81	44.16	33.86
32X-3, 96-97	297.16	10.30	5.14	7.62	2.71	2.01	2.82	45.50	36.91
32X-4, 57-58	298.27	11.25	5.51	8.75	3.16	2.04	2.77	41.88	29.94
32X-5, 10-11	298.94	14.05	7.21	10.36	3.77	1.95	2.75	46.59	37.40
33X-1, 78-79	303.58	10.89	5.43	8.19	2.99	2.01	2.75	43.06	34.56
33X-2, 130-131	305.60	9.79	4.93	7.33	2.64	1.99	2.78	45.37	35.19
33X-3, 83-84	306.63	8.96	4.51	6.76	2.46	1.99	2.76	44.41	34.14
33X-4, 114-115	308.44	12.68	6.08	10.17	3.76	2.08	2.71	37.04	25.82
33X-5, 106-107	309.86	10.16	5.07	7.63	2.77	2.00	2.76	43.64	34.77
33X-6, 28-29	310.58	11.55	5.55	9.06	3.31	2.08	2.74	38.52	28.76
34X-1, 45-48	312.95	10.85	5.58	7.80	2.77	1.94	2.82	48.90	41.08
35X-1, 98-99	323.18	9.74	4.92	7.13	2.55	1.98	2.81	46.41	38.44
35X-2, 70-71	324.40	10.38	5.05	7.97	2.89	2.06	2.77	40.78	31.69
35X-3, 31-32	325.51	10.75	5.51	7.81	2.80	1.95	2.80	47.81	39.53
36X-1, 80-81	332.70	10.60	4.32	6.36	2.22	2.45	2.88	23.14	70.82
36X-2, 53-54	333.93	8.20	4.17	5.99	2.05	1.97	2.93	50.66	38.77
36X-3, 94-97	335.84	11.14	5.57	8.37	3.01	2.00	2.79	44.72	34.71
36X-4, 81-82	337.21	13.94	6.99	10.58	3.75	1.99	2.83	46.27	33.29
36X-5, 79-80	338.69	12.08	5.98	9.16	3.28	2.02	2.80	43.92	33.43
149-898B-									
1H-1, 52-54	0.52	10.75	6.15	6.75	2.35	1.75	2.89	61.19	62.80
1H-2, 16-18	1.06	11.56	5.81	8.74	3.18	1.99	2.75	44.22	33.84
1H-3, 34-36	2.78	10.41	6.41	5.98	2.14	1.62	2.81	66.47	78.83
1H-4, 47-49	4.41	10.46	6.20	6.36	2.28	1.69	2.81	62.83	68.36

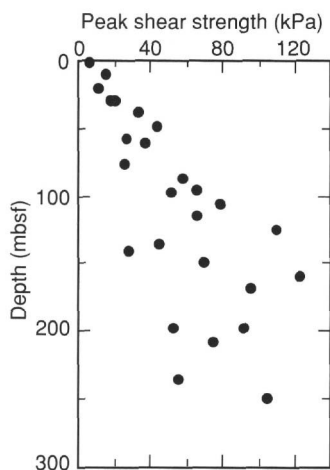


Figure 26. Undrained shear strength measurements on cores from Hole 898A.

shear strength data increases below 100 mbsf, most likely as a consequence of sampling different lithologies.

Acoustic Velocity

Discrete acoustic velocity was measured in each core recovered from Hole 898A (Table 11). No velocity measurements were performed in the single core from Hole 898B. The DSV was used for Cores 149-898A-1H to -10H to provide compressional-wave velocities in weakly consolidated sediments shallower than 95 mbsf. The Hamilton Frame Velocimeter was used to measure velocities in samples taken from Cores 149-898A-11H to -36X. Compressional-wave velocities in Cores 149-898A-11H to -36X were measured in three mutually orthogonal directions to assess the degree of acoustic anisotropy (see "Explanatory Notes" section, this volume). Repeated measurements of selected samples and calibration standards suggest an accuracy of 2% to 3% for the velocity measurements.

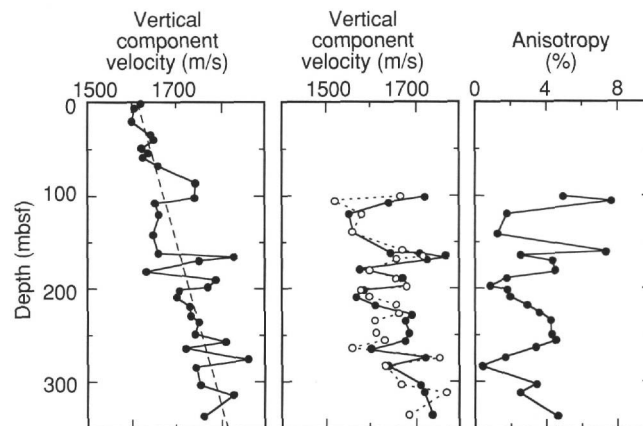


Figure 27. Hamilton Frame acoustic velocity and anisotropy measurements in cores from Hole 898A. The downhole increase in the vertical component of velocity shows a linear trend (dashed line) with a correlation coefficient of $r = 0.78$.

Discrete acoustic velocity measurements show a general increase with depth, from about 1500 m/s at the seafloor to about 1700 m/s at 340 mbsf (Fig. 27). The increase downhole in the vertical component of velocity shows a reasonably linear trend, with a slope of 0.58 s^{-1} . The correlation coefficient for the fit is 0.78, which reflects the large scatter of the downhole velocity measurements. The horizontal components of velocity show similar downhole variations. The relatively high velocities at approximately 100 and 170 mbsf were observed in all three directions. Acoustic anisotropy at these depths is approximately 8%. Anisotropy throughout the remainder of the hole is generally less than 5%, which is less than the estimated error.

Compressional velocity also was measured with the PWL tool in APC Cores 149-898A-1H to -14H. Cores below 149-898A-14H, recovered with the XCB bit, were not of the quality for reliable PWL measurements. The PWL data are shown in Figure 28, along with the linear velocity gradient derived from the discrete velocity measure-

Table 11. Discrete acoustic velocity measurements for Hole 898A.

Core, section, interval (cm)	Depth (mbsf)	Velocity (m/s)		
		V	H _x	H _y
149-898A-				
1H-2, 50-57	2.00	1514		
1H-5, 82-89	6.82	1503		
2H-2, 62-69	11.32	1504		
3H-2, 49-56	20.69	1499		
4H-5, 23-30	34.43	1539		
5H-2, 48-55	39.68	1544		
6H-2, 67-74	49.37	1521		
6H-5, 51-58	53.71	1534		
7H-2, 44-51	58.64	1524		
8H-1, 113-120	67.33	1556		
10H-1, 40-47	85.60	1640		
11H-5, 104-106	101.74	1654	1682	1738
12H-3, 44-46	107.64	1561	1532	1653
13H-5, 85-87	120.55	1592	1618	1590
16X-2, 114-116	141.44	1577	1606	1606
18X-3, 118-120	162.28	1558	1677	1646
18X-5, 107-119	165.17	1726	1721	1766
19X-2, 85-87	170.15	1647	1659	1720
20X-3, 108-110	181.48	1530	1601	1575
21X-2, 107-109	189.57	1688	1657	1674
22X-1, 128-130	197.98	1669	1680	1684
22X-4, 55-57	201.75	1606	1582	1578
23X-2, 114-116	209.04	1599	1599	1568
24X-2, 82-84	218.72	1630	1660	1611
25X-2, 94-96	228.06	1632	1664	1693
26X-1, 56-58	235.76	1648	1611	1682
27X-4, 19-21	249.49	1640	1615	1687
28X-2, 115-117	257.15	1709	1633	1681
29X-1, 96-98	265.16	1621	1565	1606
30X-1, 144-146	275.24	1762	1754	1730
31X-1, 68-70	284.18	1641	1634	1642
33X-1, 80-82	303.6	1652	1671	1712
34X-1, 46-48	312.96	1727	1771	1725
36X-3, 95-97	335.85	1661	1689	1739

ments. Data having poor signal strength are not shown (see "Explanatory Notes" chapter, this volume). Above 30 to 40 mbsf, the highest PWL velocities agree well with the discrete velocity measurements. Lower PWL velocities in this interval represent measurements taken in sections of core that had been disturbed by drilling or that contained visible gas bubbles and, therefore, are not considered representative of the sediment velocities. PWL velocities below 40 mbsf are systematically lower than the discrete velocity measurements. Possible reasons for this discrepancy include increased gas content in the core, which would reduce PWL velocities, and biased sampling for the discrete velocity measurements. Sample bias occurred because velocity measurements were taken in sediment that was sufficiently coherent to withstand either the insertion of the DSV transducers or removal of the sample for measurement in the Hamilton Frame Velocimeter. This resulted in preferential sampling of clay and ooze. PWL measurements were taken before the core liner was split and, therefore, also included incoherent sand and silt.

Magnetic Susceptibility

Magnetic susceptibility was measured at intervals of 3 to 5 cm in all cores collected at Site 898. The results are discussed in the "Paleomagnetism" section (this chapter).

Thermal Conductivity

Thermal conductivity was measured in alternate sections of all cores from Site 898. The mean error was estimated as ± 0.2 W/(m·K). Thermal conductivity values increase slightly with depth about a linear trend of 1.1 W/(m·K) at the seafloor to 1.5 W/(m·K) at 340 mbsf (Fig. 29; Table 12). This increase most likely is the result of reduced porosity arising from compaction. From 0 to 50 mbsf, most measurements lie near 1.25 W/(m·K). Between 50 and 140 mbsf, the values exhibit a large scatter about 1.4 W/(m·K). At 140 mbsf, thermal

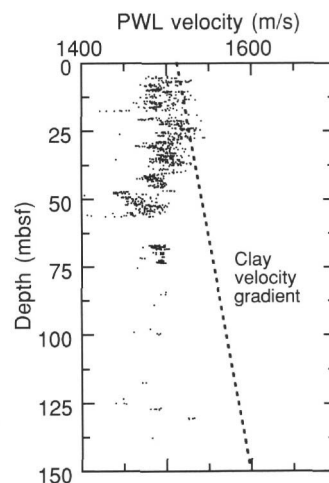


Figure 28. PWL acoustic velocity measurements in cores from Hole 898A. PWL data (dots) were sorted to eliminate data that had poor signal strength; only measurements when signal amplitude exceeded 1000 (arbitrary units) are plotted. The clay velocity gradient (dashed line) is the linear velocity gradient that was estimated from the discrete velocity measurements taken with the DSV and Hamilton Frame Velocimeter.

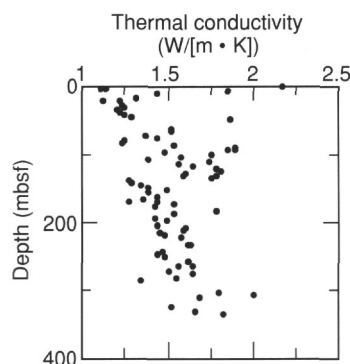


Figure 29. Thermal conductivity measurements on cores from Holes 898A and 898B.

conductivity abruptly decreases to 1.2 W/(m·K). Below this depth, a consistent increase of conductivity with depth to about 1.6 W/(m·K) at 280 mbsf can be observed. The measurements are more scattered again below 280 mbsf.

INTEGRATION OF SEISMIC PROFILES WITH OBSERVATIONS FROM THE SITE

Two multichannel seismic-reflection profiles were obtained across the site before the Leg 149 cruise began (Fig. 1 in "Background and Scientific Objectives" section, this chapter; Fig. 3, in "Site Geophysics" section, this chapter). These profiles indicated a number of reflectors that have been recognized on a regional scale in the vicinity of the Iberia Abyssal Plain and that have been dated by tracing them back to Leg 103 sites west of Galicia Bank (Mauffret and Montadert, 1988) and to Site 398 near Vigo Seamount (Groupe Galice, 1979). Lusigal Line 12 crosses the site in an east-west direction and best shows the characteristics of these reflectors and the intervening acoustic formations 1A, 1B, and 2 (Groupe Galice, 1979). The upper reflector corresponds to the 1A/1B boundary and marks a regional unconformity produced by the Miocene folding that accompanied the Rif-Betic compressional episode to the south. The middle reflector corresponds

Table 12. Thermal conductivity data from Holes 898A and 898B.

Core	Depth (mbsf)	Thermal conductivity (W/[m·K])
149-898A-		
1H-4	5.15	1.81
1H-5	6.76	1.01
1H-6	8.15	1.09
2H-2	11.40	1.57
2H-4	14.40	1.26
3H-2	20.85	1.17
3H-4	23.85	1.03
3H-6	26.85	1.16
4H-4	33.40	1.10
4H-6	36.40	1.17
5H-2	39.95	1.08
5H-4	42.95	1.15
5H-6	45.95	1.12
6H-2	49.40	1.14
6H-4	52.40	1.58
8H-2	68.45	1.32
8H-4	71.45	1.33
9H-2	77.95	1.21
9H-4	81.06	1.26
9H-6	84.06	1.18
10H-2	87.30	1.17
10H-4	90.30	1.34
10H-6	93.30	1.59
11H-2	96.80	1.58
11H-4	99.80	1.74
11H-6	102.45	1.18
12H-2	106.40	1.50
12H-4	109.40	1.47
12H-6	112.40	1.12
13H-2	116.00	1.49
13H-4	119.00	1.35
13H-6	122.00	1.29
14H-2	125.40	1.52
14H-4	128.40	1.54
14H-6	131.40	1.48
15X-2	135.00	1.52
15X-4	137.80	1.48
16X-1	139.55	1.49
16X-3	142.55	1.21
16X-5	145.35	1.06
17X-2	150.75	1.18
17X-4	153.75	1.22
17X-6	156.82	1.19
18X-2	160.35	1.21
18X-6	166.35	1.35
19X-2	170.05	1.20
19X-4	173.15	1.21
19X-6	176.05	1.16
20X-2	179.60	1.33
20X-4	182.60	1.25
21X-2	189.15	1.52
21X-4	192.15	1.43
22X-2	198.90	1.25
22X-4	201.90	1.30
23X-2	208.60	1.26
23X-4	211.60	1.39
23X-6	214.60	1.48
24X-2	218.60	1.27
24X-4	221.60	1.39
25X-2	227.77	1.37
26X-1	235.80	1.40
26X-2	237.30	1.39
27X-2	247.00	1.28
27X-4	250.05	1.26
27X-6	253.05	1.38
28X-4	259.85	1.40
29X-2	266.40	1.41
29X-4	269.45	1.46
30X-2	276.00	1.32
30X-4	278.97	1.52
31X-2	285.67	1.34
31X-4	288.70	1.18
32X-2	305.10	1.53
33X-4	308.10	1.83
34X-1	313.20	1.44
35X-3	325.60	1.21
36X-2	334.10	1.42
36X-4	337.10	1.55
149-898B-		
1H-3	3.04	1.20
1H-4	4.54	1.12

Table 13. Depths of reflectors in Hole 898A.

Reflector	Time (s TWT)	Computed depth (mbsf)	Estimated depth (mbsf)	Origin of reflector
e.g. R1	0-200			Impedance contrasts at bases of turbidites
R2	0.21	200	ca.170	Physical and lithological changes at mid-Miocene hiatus/unconformity; acoustic formation 1A/1B boundary.
R3	0.35	320	<340	Top of inclined reflector sequence
R4	0.46	430	(?)	Base of inclined reflector sequence
R5	0.61	570	(?)	Acoustic formation 1B/2 boundary
Basement	0.89	870	(?)	Top of acoustic basement

to the formation 1B/2 boundary (approximately Eocene/Oligocene) and the lowest reflector to the formation 2/3 boundary (approximately Albian/Santonian). The acoustic basement is clearly seen at the base of the sedimentary section. Two additional reflectors, which occur locally around the site within acoustic formation 1B, mark the top and bottom of a sequence of prograding reflectors (see "Site Geophysics" section, this chapter).

No downhole seismic velocity measurements were obtained at Site 898, nor did coring continue deeper than 342 mbsf. Therefore, it is not possible to correlate directly between the time of reflectors seen in the seismic-reflection profiles and the various observations in cores that are referred to depth downhole. However, the results of two sonobuoy lines shot over the Iberia Abyssal Plain (Whitmarsh, Miles, and Mauffret, 1990) could be used to convert from two-way traveltime to depth (Fig. 66, "Site 897" chapter, "Integration of Seismic Profiles with Observations from the Site" section, this volume). Thus, we estimated the downhole depths of the reflectors seen in the Lusigal Line 12 seismic-reflection profile.

Part of the Lusigal Line 12 seismic section across Site 898 is presented in Figure 30, at an enlarged scale. The 1A/1B boundary is the only regional reflector that can be correlated with observations in cores. Reflector times were picked at the onset of the relevant positive pulse. One should remember that (1) the vertical resolution of the seismic profiles is approximately equal to a quarter wavelength of the predominant energy (i.e., about 15 m) and (2) the computation of reflector depth from two-way traveltime is not more accurate than 10 m.

The causes of the reflectors at the base of the turbidite sequence and at the top of the inclined reflector sequence were investigated using their computed depths and lithologic observations of and physical measurements in cores. The times and depths of all main reflectors at this site are summarized in Table 13.

1. Many reflectors can be seen in the uppermost 200 m of the section (e.g., R1) from which cores containing sand, silty sand, and silt were obtained. These lithologies are associated with the bases of numerous turbidites, and it is likely that the contrasts in acoustic impedance at the bases of the turbidites make a substantial contribution to the reflection of sound. The reflectors are more likely to correspond to the net acoustic interference pattern produced by the series of turbidites than to individual turbidites, which are much thinner than a seismic wavelength.

2. Reflector R2 (associated with the acoustic formation 1A/1B unconformity and computed to be at 200 mbsf) can be recognized in the vicinity of the site principally from the angular relationship between the tilted and folded underlying, and horizontal onlapping, reflectors. Reflector R2 may correlate with the onset at this site of a middle Miocene to late Pliocene/earliest Pleistocene hiatus that occurs somewhere between 158 and 164 mbsf. Measurements of physical properties only tentatively suggest a physical cause for this acoustic event; velocity appears to show a small stepwise increase of about 0.1 km/s at about 165 mbsf. The lithology shows a change from terrigenous turbidites above 163 mbsf to calcareous contourites and terrigenous turbidites below 172 mbsf, which correlates only poorly with the computed depth of the reflector. Nevertheless, all the above indicators are consistent for placing the reflector between 158 and 172

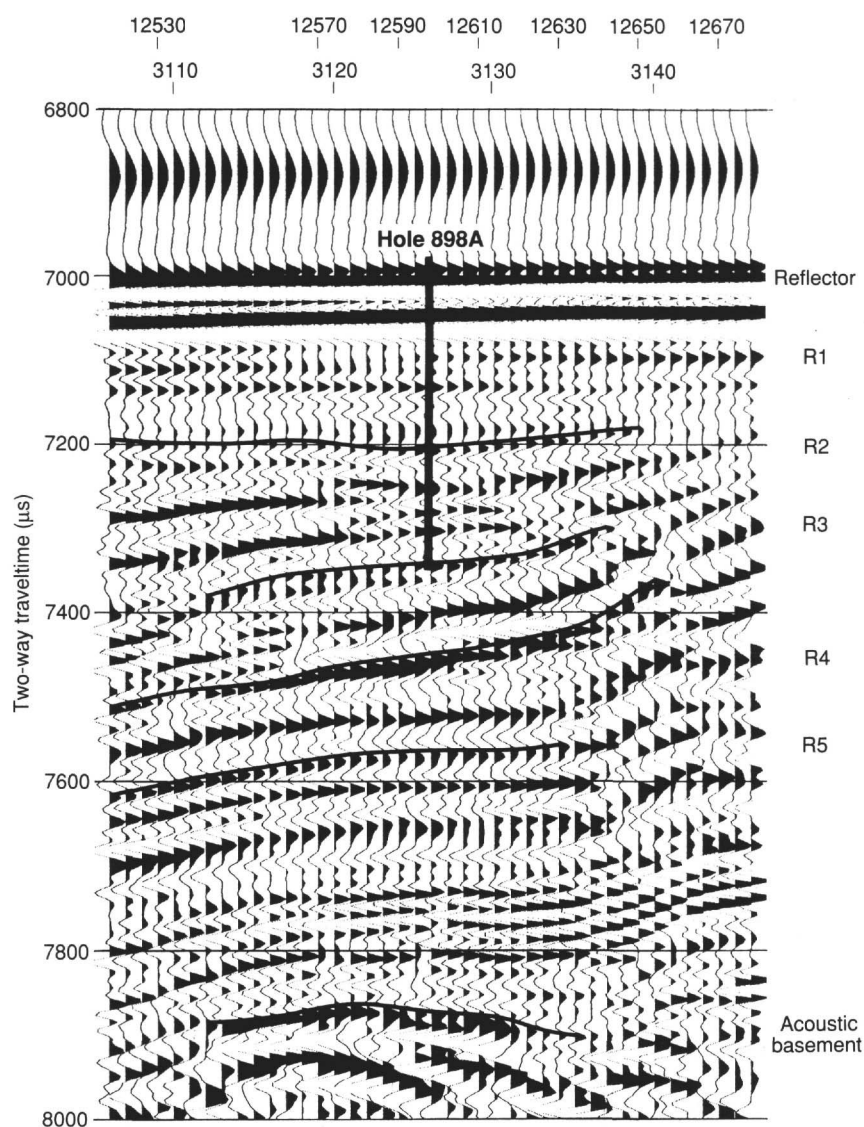


Figure 30. Expanded seismic reflection profile section from Lusigal Line 12 showing the principal reflectors R1, R2, etc., which are referred to in the text.

mbsf; this correlation was adopted here and implies an interval velocity of about 1.64 km/s from 0 to 172 mbsf.

3. Reflector R3 was computed as being at a depth of 320 mbsf. This reflector is evident in reflection profiles because of the change in the attitude of reflectors below it (i.e., they have an inclined west- or southwest-dipping sigmoidal aspect). Measurements of physical properties do not suggest a physical cause for this acoustic event, nor do the cores indicate any significant change in lithology to explain the unusual nature of the reflectors. It seems probable that when coring stopped at 342 mbsf, the bit must have passed the top of the prograding reflector sequence (the implied interval velocity for the R2/R3 interval is already high should R3 be located at 342 mbsf). However, the hole may have intersected an intervening, less reflective bed and may not have been deep enough to intersect one of the dipping beds, giving rise to the inclined reflectors, even though it had entered the inclined reflector formation itself.

IN-SITU TEMPERATURE MEASUREMENTS

The ADARA tool was deployed to collect in-situ temperature data at 113.7 mbsf in Hole 898A (ADARA depth is based on the sub-bottom depth of the bottom of the APC core barrel). The WSTP tool was

deployed to collect in-situ temperature data at 177.4 and 225.6 mbsf in Hole 898A (WSTP depth is based on the sub-bottom depth of the bottom of the previous core barrel). We did not use the WSTP measurement at 225.6 mbsf because after insertion of the tool the temperature profile did not show a normal decay toward equilibrium. This suggests that the tool was moved after insertion.

Interpretation of data from the ADARA tool deployed at 113.7 mbsf yielded a bottom-water temperature of $2.0^{\circ} \pm 0.1^{\circ}\text{C}$ and an in-situ temperature of $6.8^{\circ} \pm 0.1^{\circ}\text{C}$ (error estimates for bottom-water and in-situ temperatures are informed guesses; Fig. 31). We estimated the bottom-water temperature by averaging the observed temperature between 2100 and 2900 s, when the tool was stopped just above the seafloor. The in-situ temperature was extrapolated by using 3465 s as the insertion time and by modeling the data over the interval from 3560 to 4240 s.

Analyses of the WSTP measurements at 177.4 mbsf yielded a bottom-water temperature of $3.7^{\circ} \pm 0.1^{\circ}\text{C}$ (we address the inconsistent bottom-water temperatures below) and an in-situ temperature of $10.9^{\circ} \pm 0.1^{\circ}\text{C}$ (Fig. 32). The bottom-water temperature was obtained by averaging temperature readings between 1950 and 2100 s, when the tool was stopped just above the seafloor. The in-situ temperature was extrapolated by using 3643 s as the insertion time and by model-

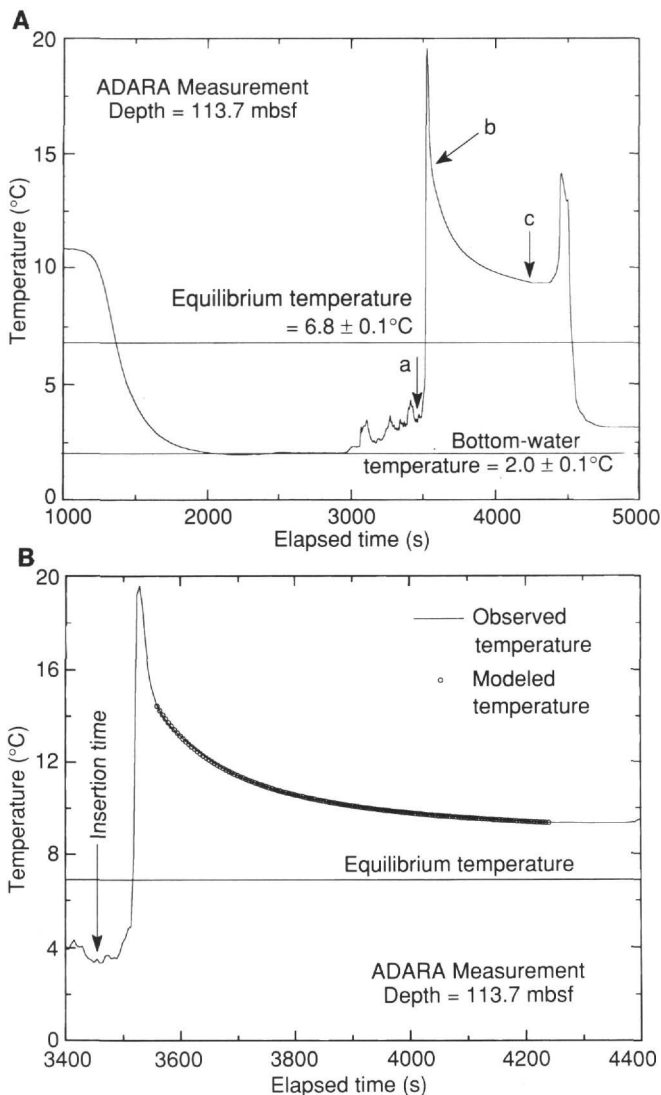


Figure 31. ADARA deployment at 113.7 mbsf in Hole 898A. **A.** Observed temperature as a function of time. The bottom-water temperature was interpreted as being $2.0^{\circ} \pm 0.1^{\circ}\text{C}$ and the in-situ temperature as being $6.8^{\circ} \pm 0.1^{\circ}\text{C}$ (these temperatures were later increased by 1.7°C to bring the ADARA and WSTP bottom-water readings into agreement). The insertion time used for curve fitting is indicated by arrow a. The portion of the temperature data used in the extrapolation is between arrows b and c. **B.** Observed temperature plotted vs. time. The quality of the temperature extrapolation is reflected in the fit of the modeled temperature to the observed temperature.

ing the data over the interval from 3661 to 3905 s. The shape of the temperature data curve suggests that the tool was inserted cleanly and also that the tool was stationary during the measurement.

The two measurements yield different estimates of bottom-water temperature. We attribute this difference to a calibration problem in the ADARA instrument. Temperature differences recorded by this instrument are likely to be more accurate than each absolute temperature. We corrected for this difference by shifting the bottom-water and in-situ temperatures recorded by the ADARA by an amount that brings the two bottom-water temperature measurements into agreement. In Table 14, therefore, we have increased the ADARA in-situ measurement by 1.7°C . This shift makes the in-situ temperature at 113.7 mbsf, $8.5^{\circ} \pm 0.1^{\circ}\text{C}$. When the ADARA instrument number 11 is next recalibrated it may be possible to improve these estimates.

Table 14. ADARA and WSTP temperature measurements and vertically integrated thermal resistivity data.

Depth (mbsf)	Temperature ($^{\circ}\text{C}$)	Vertically integrated thermal resistivity ($\text{m}^2 \text{K/W}$)
0	3.7 ± 0.1	0
113.7	8.5 ± 0.1	77.4
176.4	10.9 ± 0.1	119.3

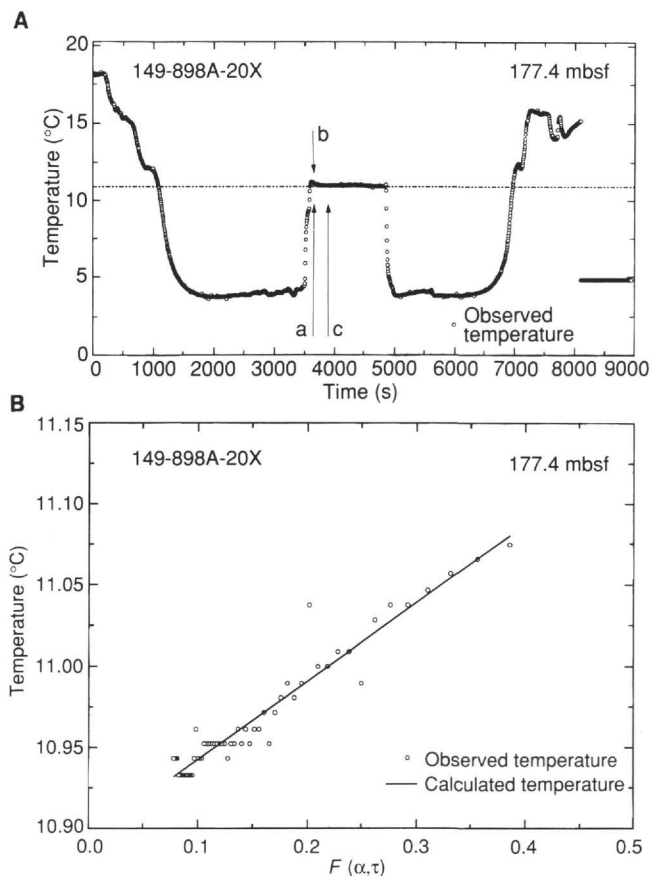


Figure 32. WSTP deployment at 177.4 mbsf in Hole 898A. **A.** Observed temperature as a function of time. The bottom-water temperature was interpreted as being $3.7^{\circ} \pm 0.1^{\circ}\text{C}$ and the in-situ temperature as $10.9^{\circ} \pm 0.1^{\circ}\text{C}$. The insertion time used for curve fitting is indicated by arrow a. The portion of the temperature data used in the extrapolation is between arrows b and c. **B.** Observed temperature plotted vs. Bullard's "F" function (Bullard, 1954). The quality of the temperature extrapolation is reflected in the linearity of the plotted points.

The slope of a linear least-squares fit of the temperature to depth (Table 14) yields an estimate of $41 \pm 2 \text{ mK/m}$ (95% confidence level) for the temperature gradient in the upper 177 mbsf at Site 898. The slope of a linear least-squares fit of the temperature to vertically integrated thermal resistivity (Table 14) yields an estimate of $61 \pm 2 \text{ mW/m}^2$ (95% confidence level) for the heat flow (see "Explanatory Notes" chapter, this volume).

SUMMARY AND CONCLUSIONS

Site 898 is situated in the Iberia Abyssal Plain over a basement ridge (Fig. 2, "Site 897" chapter, "Background and Scientific Objec-

tives" section, this volume) within the presumed ocean/continent transition (OCT) zone off western Iberia (see "Introduction" chapter, this volume). The site is one of a transect of drill sites across the OCT designed to study the petrological changes in basement rocks within the OCT, as a means of identifying the processes that accompanied continental breakup and the onset of steady-state seafloor spreading. Site 898 is located to sample a basement high between the thin oceanic crust to the west and the weakly magnetized thinned continental crust to the east (see Fig. 4 in "Introduction" chapter, this volume). The site is located within an intermediate zone of high magnetization and smooth acoustic basement, which is located between the latter two crustal types. The basement high under the site is roughly elliptical in plan view with a steep northern slope, and its shape contrasts strongly with the linear north-south basement ridges west of Site 897 (Fig. 2, "Site 897" chapter, "Background and Scientific Objectives" section, this volume). Two APC/XCB holes (one of which obtained only a mud-line core) were drilled to test this hypothesis at 40°41.1'N, 12°07.4'W, with the primary scientific objective of penetrating basement to a depth sufficient to firmly establish its character. Cores were obtained from Holes 898A and 898B that penetrated up to 342 m of Pleistocene to late Oligocene sediments. Operations were abruptly terminated with the loss of about 3340 m of drill pipe while retrieving pipe in a storm. This meant that insufficient drill pipe remained on board the ship for us to core a significant basement section at this site.

The oldest sedimentary unit cored at this site is a 176-m-thick sequence of late Oligocene to middle Miocene claystones and siltstones (Unit II), mostly deposited as calcareous contourites or turbidites at a rate of about 10 m/m.y. The likely contourite nature of the upper part of these deposits is emphasized by the hummocky appearance of the corresponding acoustic formation within acoustic formation 1B, seen in an east-west reflection profile across the site (Fig. 1). Shipboard examination of seismic profiles around the Leg 149 drill sites revealed a deeper layer of westward/southwestward inclined reflectors within acoustic formation 1B, which passes below the site. This is also probably part of a contourite drift, the top of which may have been cored near the base of Hole 898A. The Unit II sediments have a low remanent magnetization, and consequently, no clear magnetic polarity reversals are evident. An approximately 10-m.y. hiatus in deposition began in the middle Miocene and continued until the late Pliocene. This hiatus correlates with the angular unconformity between the regional acoustic formations 1A and 1B, defined by Groupe Galice (1979) that is visible in multichannel seismic reflection profiles across the site. The unconformity represents the onlapping of horizontally bedded turbidites onto reflectors that were folded and uplifted by northwest-southeast compression on the western Iberia margin during a compressional phase in the Betic Mountains of southern Spain and structural inversion in the Lusitanian Basin of Portugal.

A change in lithology occurred at the end of the hiatus, when 163 m of late Pliocene to Pleistocene age, fine-grained terrigenous turbidites, with thin intervening layers of nannofossil clay, began to accumulate at an average of about 90 m/m.y. The sediments appear to have been deposited above the CCD. The continuous and nearly complete sediment sequence in this interval provided us with an opportunity to observe a large number of magnetic polarity intervals that might possibly reach as far back as the Gilbert Chron. During the last 1.1 Ma of this sequence, turbidites were deposited at an average rate of about one every 4000 yr. The reason for this sudden increase in sedimentation rate is not clear, but may possibly be related to changes in climate.

The principal results from this site can be summarized as follows:

1. Shipboard examination of seismic profiles around the Leg 149 drill sites led to the discovery of a layer of westward/southwestward inclined reflectors within acoustic formation 1B that are considered to be part of a contourite drift, the top of which may have been cored near the base of Hole 898A.

2. A significant break in the sedimentary record, starting in the middle Miocene, can be correlated with horizontally bedded turbidites that onlap onto a monoclinical fold of sediments of middle Miocene and earlier age. This hiatus can be correlated with a regional angular unconformity in seismic-reflection profiles that may be related to northwest-southeast compression on this margin during a compressional phase in the Betic Mountains in southern Spain and structural inversion in the Lusitanian Basin of Portugal.

3. Unit I consists of 163 m of terrigenous turbidites deposited during the last 1.8 Ma. During the most recent at 1.1 Ma, at least 260 turbidites were deposited at an average of one turbidite about every 4000 yr.

4. Unit II consists of claystones and nannofossil claystones, with subsidiary sandstones, representing turbidites and pelagic/hemipelagic sediments reworked by contour currents.

A loss of drill string prevented us from achieving our primary objective at this site and led to our premature abandonment of drilling.

REFERENCES*

- Beslier, M.-O., Ask, M., and Boillot, G., 1993. Ocean-continent boundary in the Iberia Abyssal Plain from multichannel seismic data. *Tectonophysics*, 218:383-393.
- Boyce, R.E., 1973. Physical properties—methods. In Edgar, N.T., Saunders, J.B., et al., *Init. Repts. DSDP*, 15: Washington (U.S. Govt. Printing Office), 1115-1128.
- Bullard, E.G., 1954. The flow of heat through the floor of the Atlantic Ocean. *Proc. R. Soc. London A*, 222:408-429.
- Claypool, G.E., and Kvenvolden, K.A., 1983. Methane and other hydrocarbon gases in marine sediment. *Annu. Rev. Earth Planet. Sci.*, 11:299-327.
- Comas, M.C., and Maldonado, A., 1988. Late Cenozoic sedimentary facies and processes in the Iberian Abyssal Plain, Site 637, ODP Leg 103. In Boillot, G., Winterer, E.L., et al., *Proc. ODP, Sci. Results*, 103: College Station, TX (Ocean Drilling Program), 635-655.
- Emerson, S., and Hedges, J.I., 1988. Processes controlling the organic carbon content of open ocean sediments. *Paleoceanography*, 3:621-634.
- Espitalié, J., Madec, M., Tissot, B., Mennig, J.J., and Leplat, P., 1977. Source rock characterization method for petroleum exploration. *Proc. 9th Annu. Offshore Technol. Conf.*, 3:439-448.
- Folk, R.L., 1980. *Petrology of Sedimentary Rocks*: Austin (Hemphill Publ.).
- Gard, G., and Backman, J., 1990. Synthesis of Arctic and Subarctic coccolith biochronology and history of North Atlantic drift water influx during the last 500,000 years. In Bleil, U., et al. (Eds.), *Geologic History of the Polar Oceans: Arctic versus Antarctic*. NATO ASI Ser. C., 417-436.
- Gealy, E.L., 1971. Saturated bulk density, grain density, and porosity of sediment cores from the western Equatorial Pacific: Leg 7. In Winterer, E.L., Riedel, W.R., et al., *Init. Repts. DSDP*, 1: Washington (U.S. Govt. Printing Office), 1081-1104.
- Gieskes, J.M., 1974. Interstitial water studies, Leg 25. In Simpson, E.S.W., Schlich, R., et al., *Init. Repts. DSDP*, 25: Washington (U.S. Govt. Printing Office), 361-394.
- , 1983. The chemistry of interstitial waters of deep-sea sediments: interpretation of deep-sea drilling data. In Riley, J.P., and Chester, R. (Eds.), *Chemical Oceanography* (Vol. 8): London (Academic Press), 222-269.
- Groupe Galice, 1979. The continental margin off Galicia and Portugal: acoustical stratigraphy, dredge stratigraphy, and structural evolution. In Sibuet, J.-C., Ryan, W.B.F., et al., *Init. Repts. DSDP*, 47 (Pt. 2): Washington (U.S. Govt. Printing Office), 633-662.
- Hamilton, E.L., 1976. Variations of density and porosity with depth in deep-sea sediments. *J. Sediment. Petrol.*, 46:280-300.
- Iaccarino, S., and Salvatorini, G., 1979. Planktonic foraminiferal biostratigraphy of Neogene and Quaternary of Site 398 of DSDP Leg 47B. In Sibuet, J.-C., Ryan, W.B.F., et al., *Init. Repts. DSDP*, 47 (Pt. 2): Washington (U.S. Govt. Printing Office), 255-285.
- Kennett, J.P., and Srinivasan, M.S., 1983. *Neogene Planktonic Foraminifera: A Phylogenetic Atlas*: Stroudsburg, PA (Hutchinson Ross).

*Abbreviations for names of organizations and publication titles in ODP reference lists follow the style given in *Chemical Abstracts Service Source Index* (published by American Chemical Society).

- Martini, E., 1971. Standard Tertiary and Quaternary calcareous nannoplankton zonation. In Farinacci, A. (Ed.), *Proc. 2nd Int. Conf. Planktonic Microfossils Roma*: Rome (Ed. Tecnosci.), 2:739-785.
- Mauffret, A., and Montadert, L., 1988. Seismic stratigraphy off Galicia. In Boillot, G., Winterer, E.L., et al., *Proc. ODP, Sci. Results*, 103: College Station, TX (Ocean Drilling Program), 13-30.
- McIver, R., 1975. Hydrocarbon occurrence from JOIDES Deep Sea Drilling Project. *Proc. Ninth Petrol. Congr.*, 269-280.
- Meyers, P.A., in press. Preservation of source identification of sedimentary organic matter during and after deposition. *Chem. Geol.*
- Meyers, P.A., and Brassell, S.C., 1985. Biogenic gases in sediments deposited since Miocene times on the Walvis Ridge, South Atlantic Ocean. In Caldwell, D.E., Brierly, J.A., and Caldwell, C.L. (Eds.), *Planetary Ecology*: New York (Wiley), 69-80.
- Müller, P.J., 1977. C/N ratios in Pacific deep sea sediments: effect of inorganic ammonium and organic nitrogen compounds sorbed by clays. *Geochim. Cosmochim. Acta*, 41:765-776.
- Rio, D., Raffi, I., and Villa, G., 1990. Pliocene-Pleistocene calcareous nannofossil distribution patterns in the Western Mediterranean. In Kastens, K.A., Mascle, J., et al., *Proc. ODP, Sci. Results*, 107: College Station, TX (Ocean Drilling Program), 513-533.
- Rothwell, R.G., Pearce, T.J., and Weaver, P.P.E., 1992. Late Quaternary evolution of the Madeira Abyssal Plain, Canary Basin, NE Atlantic. *Basin Res.*, 4:103-131.
- Sayles, E.L., Manheim, F.T., and Waterman, L.S., 1973. Interstitial water studies on small core samples, Leg 20. In Heezen, B.C., MacGregor, I.D., et al., *Init. Repts. DSDP*, 20: Washington (U.S. Govt. Printing Office), 871-874.
- Shipboard Scientific Party, 1990. Site 767. In Rangin, C., Silver, E.A., von Breyman, M.T., et al., *Proc. ODP, Init. Repts.*, 124: College Station, TX (Ocean Drilling Program), 121-193.
- Sibuet, J.-C., Ryan, W.B.F., et al., 1979. *Init. Repts. DSDP*, 47 (Pt. 2): Washington (U.S. Govt. Printing Office).
- Snowdon, L.R., and Meyers, P.A., 1992. Source and maturity of organic matter in sediments and rocks from Sites 759, 760, 761, and 764 (Wombat Plateau) and Sites 762 and 763 (Exmouth Plateau). In von Rad, U., Haq, B.U., et al., *Proc. ODP, Sci. Results*, 122: College Station, TX (Ocean Drilling Program), 309-315.
- Stow, D.A.V., and Piper, D.J.W., 1984. Deep-water fine-grained sediments: facies models. In Stow, D.A.V., and Piper, D.J.W. (Eds.), *Fine-grained Sediments: Deep-Water Processes and Facies*: Oxford (Blackwell), 15:611-645.
- Suess, E., 1980. Particulate organic carbon flux in the oceans—surface productivity and oxygen utilization. *Nature*, 288:260-263.
- Whitmarsh, R.B., Miles, P.R., and Mauffret, A., 1990. The ocean-continent boundary off the western continental margin of Iberia, I. Crustal structure at 40°30'N. *Geophys. J. Int.*, 103:509-531.
- Whitmarsh, R.B., Pinheiro, L.M., Miles, P.R., Recq, M., and Sibuet, J.C., 1993. Thin crust at the western Iberia ocean-continent transition and ophiolites. *Tectonics*, 12:1230-1239.

Ms 149IR-105

NOTE: For all sites drilled, core-description forms ("barrel sheets") and core photographs have been reproduced on coated paper and can be found in Section 3, beginning on page 271. Forms containing smear-slide data can be found in Section 4, beginning on page 657. GRAPE, Index Property and MAGSUS data are presented on CD-ROM (back pocket).